2013 (Heisei 25)

Doctoral Thesis

Aero-thermodynamic Consideration of Nonrotating Components for Single-Crystal Silicon Microscale Turbine Engine

RITSUMEIKAN UNIVERSITY

GRADUATE SCHOOL OF SCIENCE AND ENGINEERING

DOCTORAL PROGRAM IN INTEGRATED SCIENCE AND ENGINEERING

Moriaki Namura

Contents

List of figure captions

List of figure captions in chapter 2

List of figure captions in chapter 3

List of figure captions in chapter 4

Lefebvre's θ parameters ($\theta \equiv \frac{(P_6)^{1.75} A_{ref} (L_{ref})^{0.75} \exp(T_6/300)}{\dot{m}_A}$)[8]

Fig.4.5 Comparison of predictions and experimental results for stable combustion operating spaces obtained from past and present works (previous works were reported by MIT [11-14] and SIMTEC [9])

List of figure captions in Appendix A

List of table caption

List of table caption in chapter 2

List of table caption in chapter 3

Nomenclature

A = area

A_f = flame area

C = dynamic head

C_p = constant pressure specific heat

d = diameter

Da = Damköhler number

h = enthalpy

H = lower specific energy of fuel

K=Boltzmann constant

Kn= Knudsen number

L = characteristic length

M = Mach number

$\dot{m}$ = mass flow rate

Nu =Nusselt number

Pr= Prandtl number

p = pressure

ΔP = pressure drop

q = fuel/air ratio by mass

Q = amount of heat

R = gas constant

$\bar{R}$ = universal gas constant

Re = Reynolds number

S = burning velocity

T = temperature

u = velocity

x = characteristic channel length

μ = gas viscosity

γ = specific heat ratio

λ = mean free path

$\nu(M)$ = Prandtle-Meyer function

ρ = density

ϕ = equivalence ratio

η_c = combustion efficiency

η_i = combustion inefficiency

$\tau_{chemical}$ = characteristic chemical time

Subscripts

0 = stagnation state

A= air

aw = adiabatic wall

Cf = frictional coefficient

exp = experiment

f = fuel

ft = flame-tube

H = hydraulic

in= inlet station of control volume

j = primary zone air jets

L = laminar flow

out= outlet station of control volume

ref = reference scale

T = turbulent flow

w = wall

1= nozzle inlet station

* = throat station

3= nozzle outlet station

∞ = core flow

4= inlet station of flame sheet

5 = outlet station of flame sheet

6= combustor inlet station of Brayton cycle

Chapter 1

Introduction

1.1 Motivation and Objectives

1.1.1 Motivation and Objectives for Microscale Internal Flow Devices

For many microscale fluid devices of engineering importance, the fluid motion is appropriately characterized as an internal flow. Examples of such devices are microscale gas turbine engines, microscale thrusters for propulsion systems, and microscale fluid machinery components, such as compressors, turbines, combustors, nozzles, and diffusers [1-14]. However, the aerodynamic behavior of microscale compressible internal flows has not yet been clarified sufficiently. As a historical breakthrough in the investigation of the aerodynamics of large-scale compressible internal flows, a simple convergent-divergent nozzle, the so-called Laval nozzle, has been adopted [15,16]. The fundamental concept of the aerodynamics of a microscale compressible internal flow is expected to be similar to that of the large-scale counterpart. Indeed, many studies on microscale Laval nozzle devices have been reported to date [4-14]. However, these devices have different dimensions and configurations [4-14], which prevents the establishment of unified aerodynamic design guidelines that are important for engineering practice.

In this paper, the design, microfabrication, and direct measurement of the static pressure distribution for the aerodynamics of a single-crystal-silicon microscale supersonic nozzle are described. The microscale supersonic nozzle has a convergent-divergent section and a throat area of 100 μm × 300 μm. The microscale supersonic nozzle was fabricated using silicon bulk micromachining technology. The degree of rarefaction of the nozzle flow was determined by the Knudsen number (Kn). The operation envelope, which determines whether the continuum or rarefied flow assumption is appropriate, can be expressed as a function of Kn and related parameters. The effect of nonadiabatic operation on a microscale nozzle flow was investigated on the basis of wall heat transfer. These physical correlations were taken into account for the classical Shapiro equations to analyze the microscale nozzle flow aerodynamics [15]. Furthermore, the solutions of Shapiro's equations were compared with experimental results obtained by the authors and other research institutions to demonstrate the validity of the proposed aerodynamic design concept for a microscale continuum flow.

Therefore, it is suggested from an engineering viewpoint that a quantitative aerodynamic

evaluation based on Kn and nonadiabatic operation can provide practical aerodynamic design guidelines for microscale continuum internal flow devices with different dimensions and configurations.

1.1.2 Motivation and Objectives for Microscale Combustors

An excellent review by Epstein of Massachusetts Institute of Technology (MIT) described the technical challenges of mm-scale silicon gas turbine engines for portable electric power generation and microscale air vehicle propulsion systems [1]. Microscale rotating and nonrotating components for a microscale gas turbine engine such as a centrifugal compressor, annular combustor, and radial inflow reaction turbine have been developed to satisfy the required specifications based on the Brayton cycle.

This paper describes the aero-thermodynamic design, microfabrication, and combustion test results for a single-crystal-silicon premixed-fuel microscale can combustor. The combustion chamber volume is 277 mm^3 and the microscale can combustor was fabricated using silicon bulk micromachining technology. Hydrogen fuel-air premixing was performed in the combustion test. The operation space in which stable combustion occurred was experimentally determined from the combustion temperature and efficiency for various mass flow rates and equivalence ratios. The expression for the combustion efficiency under conditions where the overall rate of heat release is limited by the chemical kinetics was consistent with the burning velocity model. The flame stabilization, the range of equivalence ratios, and the maximum air velocity that the combustor can tolerate before flame extinction occurs were in agreement with the well-stirred reactor (WSR) and combustion loading parameter (CLP) models. A proposed aero-thermodynamic approach based on these three models will provide a physical interpretation of experimental results in the operation space of stable combustion. Furthermore, this approach provides a unified physical interpretation of the stable combustion operation spaces of microscale combustors with various dimensions and configurations. Therefore, it is demonstrated that the proposed aero-thermodynamic approach has an important role in predicting the preliminary aerodynamic design performances of new microscale combustors.

1.2 Review of Previous Work and Technical Issues

1.2.1 Review of Previous Work and Technical Issues for Microscale Internal Flow Devices

The excellent pioneering work by Bayt is considered a milestone in this field, who described the technical challenges and issues associated with microscale thruster nozzles [5,9-10].

Two micropropulsion systems were proposed by Bayt et al. One was an unheated microthruster and the other was a microthruster that can achieve an exhaust thruster temperature

of 973 K by resistively heating fins located from the chamber to the thruster inlet. Bayt manufactured the unheated microthruster using silicon microfabrication technology. It was experimentally found that 11.3 mN of thrust was generated for a 16.9:1 expansion ratio of the unheated microthruster with a 37 μm throat width and 308 μm throat depth. The exit velocity was 650 m/s, which corresponds to an exit Mach number of 4.2. Then, performances such as the specific impulse of the thruster were evaluated for the heated microthruster. As a result, Bayt showed that a reduction in the Reynolds number (Re) with increased chamber temperature causes increased viscous dissipation and reduced thruster efficiency. Therefore, the Reynolds number was considered as the dominant parameter determining the performance of these systems. These results suggest that micro-electro-mechanical systems (MEMS)-based micropropulsion systems provide higher performance of the thrust, thruster efficiency, specific impulse, and specific impulse efficiency at a relatively low device mass and mass flow rate, under operation at Re of above 2500 for both the heated and unheated thrusters [5,9-10].

On the basis of the above experimental evidence, Bayt suggested that the transition condition from Navier-Stokes equations to slip flow equations as governing equations for fluid motion can be described as a function of the Knudsen number (Kn). Kn, which is a well-known parameter that describes the degree of rarefaction of the flow region, has been applied to aerodynamic design for large-scale hypersonic and hyperaltitude vehicles [17]. For two decades, with the progress of MEMS-based silicon bulk micromachining technology, we have been able to materialize microscale-to-millimeter-scale fluid devices. Then, a new physical phenomenon was revealed, that reducing the device scale increases Kn, resulting in a low-density flow region becoming consistent with a large-scale hypersonic and hyperaltitude flow region [17].

As a result of a series of studies by Bayt et al. and other research institutions, the main technical issues in the design of microscale compressible internal flow devices have been pointed out to be as follows [4-14,18]:

(1) A microscale nozzle flow region with a Knudsen number larger than 0.1 $(0.1 < \mathrm{Kn} < 10)$ corresponds to a transition region where second-order slip or higher-order Burnett equations or molecular modeling may be introduced.
(2) Continuum Navier-Stokes equations for fluid motion with first-order slip boundary conditions are still valid for a microscale nozzle flow region with a Knudsen number of $0.001 \le \mathrm{Kn} \le 0.1$.
(3) The large surface-area-to-volume ratio of a microscale nozzle results in nonadiabatic operation. The coupling between wall heat transfer and fluid energy dissipation is an important factor in the aerodynamic design.
(4) A microscale nozzle converts stagnation enthalpy to kinetic energy. Thus, the Mach number

or static pressure is a rational parameter describing aerodynamic characteristics.

In this study, we attempt to investigate the effects of the above-mentioned technical issues on the aerodynamic design of microscale continuum internal flow devices to ensure their consistency with the results of previous studies and existing knowledge. It is expected that, from a practical engineering viewpoint, a quantitative evaluation of these effects can provide aerodynamic design guidelines for microscale nonrotating components of fluid devices, i.e., microscale nozzles, diffusers, and thrusters with different dimensions and configurations.

1.2.2 Review of Previous Work and Technical Issues for Microscale Combustors

One of the technical challenges of the MIT microscale gas turbine engine project was to develop microscale silicon annular combustors with combustion chamber volumes from 66 mm^3 to 220 mm^3.

Mehra and Waitz [19,20] described a combustion chamber with a volume of 66 mm^3 that consisted of three silicon wafer levels. For premixed hydrogen-air fuel combustion, exit gas temperatures in excess of 1800 K were achieved with combustor efficiencies of up to 70%. Spadaccini[2] described a combustion chamber with a volume of 191 mm^3 consisting of six silicon wafer levels. Premixed hydrogen-air fuel combustion was sustained at exit temperatures higher than 1600 K with efficiencies of over 90% and power densities of up to 1100 MW/m^3. Non-premixed hydrogen-air fuel combustion was also stabilized with similar performances. Furthermore, ethylene fuel-air and propane fuel-air premixtures were used in combustion tests under a wide range of equivalence ratios, and the combustor achieved efficiencies of up to 60% and power densities of approximately 500 MW/m^3 [1,2,19,20].

A fourfold increase in the power density was achieved for a platinum-nickel catalytic combustor by performing propane fuel-air premixing [21,22].

As a result of a series of studies at MIT, the overall performance and some of the combustion physics underlying microscale combustor design have been clarified. Spadaccini et al. concluded that the operation space of a microscale combustor can be expressed as a function of the Damköhler number (Da), thermal loss (combustion efficiency), and power density. Furthermore, the main technical issues in the design of microscale combustors were pointed out to be as follows [2].

(1) A high power density requires a high mass flow rate per unit volume. However, a mass flow rate with a Damköhler number of less than 1 (Da<1) induces blowoff or flame extinction.
(2) A large recirculation zone in the flameholder wake flow reduces the effective volume of the combustion chamber. This condition results in a decreased residence time and Da.

(3) The large surface area to volume ratio of a microscale combustor results in nonadiabatic operation. The coupling between heat transfer and chemical kinetics is an important factor in the design.

In this paper, we attempt to apply an aero-thermodynamic approach based on the burning velocity, well-stirred reactor (WSR), and combustion loading parameter (CLP) models to microscale combustor design. Each model has been applied to large-scale aircraft engine design because it is based on the physics of the residence and chemical reactions of fluids, and a strong correlation exists between each model and combustion test results [23]. These models take into account the dimensions, inlet static temperature, inlet static pressure, and mass flow rate of the combustor, which are useful for practical engineering design.

The proposed silicon microscale can combustor may be used in microscale turbomachinery as a future application. A hydrogen fuel-air premixture was used in the combustion tests. However, the main purpose of this paper is to provide a unified practical aero-thermodynamic design method for microscale combustors based on a rigorous physical background. To establish an aero-thermodynamic model for microscale combustors, the correlation between the geometrical scale and configuration and the aerodynamic parameters that determine the operation space of stable combustion was investigated in detail.

The three technical issues suggested by Spadaccini et al. were taken into account in the model to ensure its consistency with the results of previous studies and existing knowledge. Therefore, the model is expected to provide insight into unsolved technical issues discussed in previous works. Furthermore, the model has an important role in predicting the practical specifications of new designs of microscale combustors with unknown performance.

1.3 Scope and Outline of Thesis

The structure of this paper is as follows. In Sec.2.1, the relationship between the governing equation of fluid motion, Kn, and related parameters is briefly reviewed. A typical map of the operation envelope for microscale nozzle flows investigated by the authors and other institutions is provided on the basis of a review. This map provides rational information on whether the continuum or rarefied flow assumption is appropriate for the aerodynamic design of microscale compressible internal flow devices. Furthermore, the effects of Kn and nonadiabatic operation on a microscale compressible internal flow, which were investigated on the basis of the wall heat transfer mechanism, are shown. In Sec.2.2, the geometrical design procedure based on the method of characteristics for a microscale nozzle is described. In Secs.2.3 and 2.4, the microfabrication process for a microscale nozzle using silicon bulk micromachining technology and the experimental procedure are discussed, respectively. In

Sec.2.5, the experimental results for the direct measurement of the static pressure distribution of a nozzle flow are analyzed. In Sec.2.5, a classical Shapiro quasi-one-dimensional equation based on the Reynolds transportation theorem [15,16] is used to analyze the static pressure variation of a microscale nozzle flow and is extended to nonadiabatic operation conditions.

In Sec.3.1, the burning velocity model proposed by Lefebvre and Ballal [23] for large-scale gas turbine combustors is reviewed before its application to a microscale combustor with heat losses. As described in Sec.3.2, the microscale can combustor is divided into two zones, i.e., flameholder recirculation and flame propagation zones, to establish design guidelines for determining the aero-thermodynamic performance based on the burning velocity, WSR, and CLP models. Sec.3.3 describes the microfabrication process of the combustor using silicon bulk micromachining. Sec.3.4 describes the results of combustion experiments involving hydrogen fuel-air premixing for various mass flow rates and equivalence ratios. In Sec.3.5, it is shown that the proposed model provides a rigorous physical interpretation of the performance of the microscale combustors investigated by the authors and other research institutions [1-3,19,20,24,25].

Finally, in Chap.4, it is concluded, from a practical engineering viewpoint, that the model can provide unified design guidelines for microscale nozzles and combustors having different dimensions and configurations.

References

[1] Epstein, A. H., 2004, "Millimeter-Scale, Micro-Electro-Mechanical Systems Gas turbine Engines", J Eng Gas Turb Power- Trans ASME, vol.125, pp.205-226.

[2] Spadaccini, C.M., Mehra, A., Lee, J., Zhang, X., Lukachko, S., and Waitz, I.A., 2003, "High Power Density Silicon Combustion Systems for Micro Gas Turbine Engines", Transactions of the ASME, J Eng Gas Turb Power- Trans ASME, vol. 125, pp.709-719.

[3] Namura,M., and Toriyama,T., 2012," Aero-Thermodynamic Consideration of Single-Crystal-Silicon Premixed-Fuel Microscale Can Combustor", Transactions of the ASME, J Eng Gas Turb Power- Trans ASME, vol. 134, pp. 071501-1-071501-11.

[4] Reed, B. D., de Groot, W., and Dang, L., 2001, "Experimental Evaluation of Cold Flow Micronozzles," AIAA, Paper 2001-3521.

[5] Bayt, R. L. and Breuer, K. S., Nov.1998 "Viscous effects in supersonic MEMS-fabricated nozzles," In: Proceedings of the 1998 ASME International Mechanical Engineering Congress and Exposition, Anaheim CA. ASME. New York, pp. 117–123.

[6] Hitt, D. L., Zakrzwski, C. M., and Thomas, M. A., 2001, "MEMS-based satellite micropropulsion via catalyzed hydrogen peroxide decomposition," *Smart Mater. Struct.,* vol. 10, pp. 1163–1175.

[7] Mueller, J., Chakraborty, I., Bame, D., and Tang, W., 2000, "Vaporizing liquid microthruster concept. Preliminary results of initial feasibility studies," *in Micropropulsion for Small Spacecraft*, edited by M.Micci and A. Ketsdever, Progress in Astronautics and Aeronautics, vol. 187, pp. 215-230.

[8] London, S A. P., Epstein, A. H., and Kerrebrock, J. L., Jul.-Aug. 2001, "High-temperature bipropellant microrocket engine," Journal of Propulsion and Power, vol. 17, no. 4, pp. 780-787.

[9] Bayt, R. L, 1999, "Analysis, Fabrication and Testing of a MEMS-based Micropropulsion System", Ph.D. Thesis, Department of Aeronautics and Astronautics, MIT.

[10] Bayt, R. L and Kenneth, S.B., 2001, "Analysis and testing of a silicon intrinsic-point heater in a micropropulsion application", Sensors and Actuators A, vol. 91, pp.249-255.

[11] Arkilic, E. B., Schmidt, M. A., and Breuer, K. S., 1997, "Gaseous Slip Flow in Long Microchannels", Journal of Microelectromechanical Systems, vol.6, pp.167-178.

[12] Nagai, H., Naraoka, R., Sawada, K. and Asai, K., 2008, "Pressure-Sensitive Paint Measurement of Pressure Distribution in a Supersonic Micronozzle", AIAA Journal, vol. 46, pp. 215-222.

[13] Alexeenko, A. A., Fedosov, D. A., Gimelshein, S. F., Levin, D. A. and Collins, R. J., 2006, "Transient Heat Transfer and Gas Flow in a MEMS-Based Thruster", Journal of Microelectromechanical Systems, vol. 15, pp.181-194.

[14] Alexeenko, A. A., Levin, D. A., Fedosov, D. A., Gimelshein, S. F. and Collins, R. J., 2005, "Performance Analysis of Microthrusters Based on Coupled Thermal-Fluid Modeling and Simulation", Journal of Propulsion and Power, vol. 21, pp.95-101.

[15] Shapiro, A.H., 1953, "The Dynamics and Thermodynamics of Compressible Fluid Flow", The Ronald Press Company, Chaps.7 and 8.

[16] Greitzer, E.M., Tan, C.S., and Graf, M.B., 2006, "Internal Flow", Cambridge University Press, Chap.2 and 10.

[17] Heiser, W.H., and Pratt, D.T., 1994, "Hypersonic Airbreathing Propulsion", American Institute of Aeronautics and Astronautics Inc., Chap.2.

[18] Beskok, A., Karniadakis, G. E., 1994, "Simulation of Heat and Momentum Transfer in Complex Microgeometries", Journal of Thermophysics and Heat transfer, vol. 8, pp.647-655.

[19] Mehra, A., Zhang, X., Ayon, A.A., Waitz, I.A., Schmidt, M.A., and Spadaccini, C.M., 2000, "A Six-Wafer Combustion Systems for a Silicon Micro Gas Turbine Engine", Journal of Microelectromechanical Systems, vol. 9, pp.517-527.

[20] Waitz, I.A., Gauba, G., and Tzeng, Y.S., 1998, "Combustors for Micro - Gas Turbine Engines", Journal of Fluid Engineering, vol. 120, pp.109-117.

[21] Spadaccini, C.M., Zhang, X., Cadou, C.P., Miki, N., and Waitz, I.A., 2003, "Preliminary Development of a hydrocarbon-fueled catalytic micro-combustor", Sensors and Actuators A, vol.103, pp.219-224.

[22] Spadaccini, C.M., Peck, J., and Waitz, I.A., 2007, "Catalytic Combustion Systems formicroscale Gas Turbine Engines", Journal of Engineering for Gas Turbines and Power, vol. 129, pp.49-60.

[23] Lefebvre, A.H. and Ballal, D.R., 2010, "Gas Turbine Combustion: Alternative Fuels and Emissions", Third Edition, Taylor & Francis, pp.136-167.

[24] Shan, X.C., Wang, Z.F., Jin, Y.F., Wu, M., Hua, J., Wong, C.K., and Maeda, R., 2005, "Studies on a Micro Combustor for Gas Turbine Engines", Journal of Micromechanics and Microengineering, vo.15, pp.S215-S221.

[25] Hua, J., Wu, M., and Kumar, K., 2005, "Numerical simulation of the combustion of hydrogen-air mixture in microscaled chambers Part II: CFD analysis for a micro-combustor", Chemical Engineering Science, vo.60, pp.3507-3515.

Chapter 2

Aerodynamics of Single-Crystal Silicon Microscale Supersonic Nozzle

2.1 Operation Envelope of Microscale Nozzle Flow

2.1.1 Relationship between Governing Equation of Motion, Knudsen number (Kn) and Related Parameters

On the basis of Knudsen number for past experiments of mircoscale nozzle flow reported by other research institutions, hereafter referred to as MIT [1,2], UTRC [3], MIT (silp) [4], Tohoku [5], and Pennsylvania[6,7], an estimation to determine whether the continuum or rarefied flow assumption is appropriate for the governing equation of motion is carried out. Kn is defined as [8]

$$Kn = \frac{\lambda}{L} \quad , \tag{2.1}$$

where L is the characteristic length, and λ is the mean free path. An alternate form is [8]

$$Kn = \frac{\delta^3}{\sqrt{2}\pi d^2 L} \quad , \tag{2.2}$$

where d is the gas molecular diameter, and δ is the mean intermolecular distance. The calculation of Kn for each device reported by other research institutions is carried out using Eq. (2.2). As a first approximation, standard atmospheric conditions and throat width as the characteristic length are adopted in the calculation. Figure 2.1 shows the results of calculation. It is concluded that, apart from one exception, experimental results are located within the continuum flow region. The exception is located within the transition flow region. A more quantitative calculation can be carried out to represent the operation envelope of the governing equation of motion as a function of Kn and related parameters. The number density of gas can be described by thermodynamic states as

$$\delta^3 = \frac{KT}{p}. \tag{2.3}$$

Therefore, by combining Eqs. (2.2) and (2.3), the operation envelope of the governing equation of motion for each device can be represented as a function of the characteristic length L and gas molecular parameters L/δ, δ/d, and Kn. According to the suggestion by Bird [8], assumptions were made for calculations indicating that the upper limit of continuum flow is $Kn = 0.1$, the dense gas is $\delta/d = 7$, and the statistical flow is $L/\delta = 100$. Figure 2.2 shows a comparison of the calculated operation envelope of the governing equation of motion and experimental data. It is more quantitatively concluded that, apart from one exception, experimental results are located within the continuum flow region where a Navier–Stokes equations is valid. The exception is located within the transition flow region where the slip and accommodation flow concepts may be introduced [9].

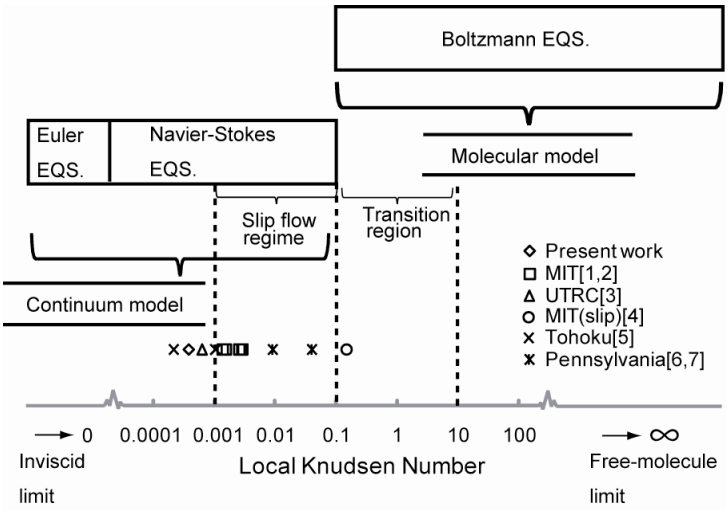

Fig.2.1 Calculation of Kn for each device reported by other research institutions (MIT [1,2], UTRC [3], MIT (silp) [4], Tohoku [5], and Pennsylvania [6,7])

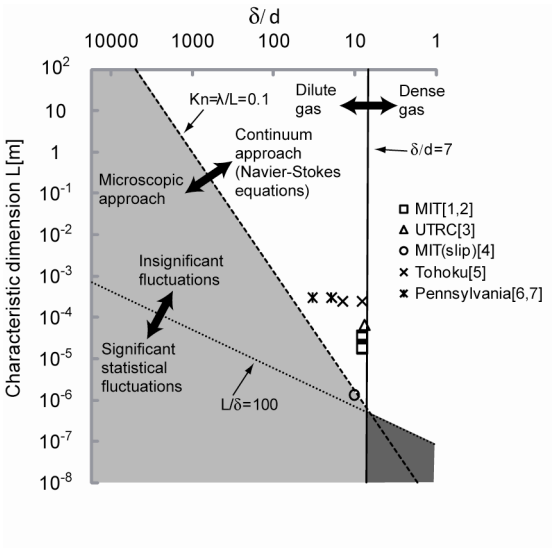

Fig.2.2 Comparison of calculated operation envelope of the governing equation of motion and experimental data (MIT [1,2], UTRC [3], MIT (silp) [4], Tohoku [5], and Pennsylvania [6,7])

2.1.2 Engineering Significance of Nonadiabatic Operation of Microscale Nozzle Flow

Applying the Reynolds analogy to laminar boundary layers, the heat transfer film coefficient can be related to the skin friction coefficient as [10,11]

$$\frac{h}{\rho u C_p} = \frac{C_f}{2}. \tag{2.4}$$

where h is heat transfer film coefficient. The Reynolds analogy is shown in more detail in Sec. 2.5.

The skin friction coefficient is a function of Reynolds number,

$$C_f \propto \frac{1}{Re^m} \propto \frac{1}{{d_H}^m} \quad (m < 1). \tag{2.5}$$

Thus, the scaling law of the heat transfer film coefficient can be expressed as follows while keeping the flow velocity constant:

$$h \propto \frac{1}{{d_H}^m} \quad . \tag{2.6}$$

This relation indicates that heat transfer is more sensitive to the hydrodynamic diameter for microscale devices. In the absence of more precise experimental data for microscale nozzle flow, it is reasonable to assume as a first approximation that a classical straight pipe heat transfer relation holds for a channel [12,13],

$$\mathrm{Nu} = 1.357\left(\frac{2x/d_H}{\mathrm{RePr}}\right)^{-1/3} \text{ for } \frac{2x/d_H}{\mathrm{RePr}} \le 0.01, \tag{2.7}$$

$$\mathrm{Nu} \cong 3.656 \quad \text{for} \quad \frac{2x/d_H}{\mathrm{RePr}} > 0.25 \quad . \tag{2.8}$$

Substituting Eq. (2.1) into Eq. (2.7), Nu can be expressed as a function of Kn,

$$\mathrm{Nu} = 1.357\left(\frac{2x\mathrm{Kn}/\lambda}{\mathrm{RePr}}\right)^{-1/3} . \tag{2.9}$$

Figure 2.3 shows the relationship between Nu and $(2x/d_H)/(\mathrm{RePr})$ calculated from Eqs. (2.7) and (2.8). Air ($\mathrm{Pr} = 0.73$) is considered in the calculation. Experimental data are plotted in the figure for comparison. It is concluded that, apart from a few exceptions, experimental results coincide with calculations. Equation (2.9) is used to determine possible reasons for the few exceptions, i.e., the discrepancy between experiment and calculation. Figure 2.4 shows the relationship between Nu and Kn calculated from Eq. (2.9). Experimental data are also plotted for comparison. It can be seen from Fig.2.4 that the discrepancy between experiment and calculation is relatively small for $0.001 \ge \mathrm{Kn}$. However, the difference is relatively large for $0.01 \le \mathrm{Kn}$. As Kn increases beyond $0.001 \le \mathrm{Kn}$, flow starts deviating from the continuum assumption. In the slip flow regime, the deviations are assumed to be not large enough in the range of $0.001 \le \mathrm{Kn} \le 0.1$, and Navier–Stokes equations with the wall slip or jump boundary conditions are still used.

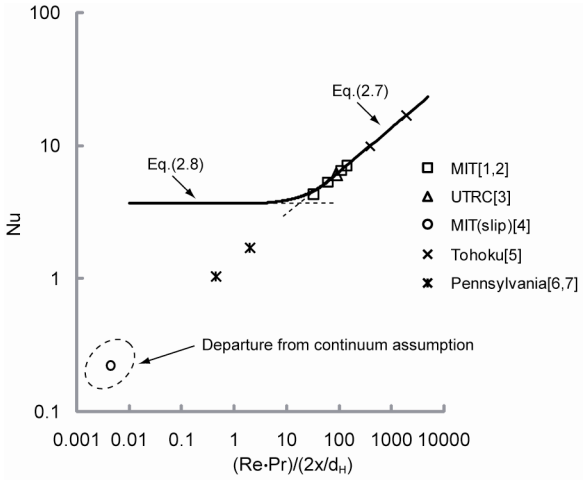

Fig.2.3 Relationship between Nu and $\frac{2x/d_H}{RePr}$ (MIT [1,2], UTRC [3], MIT (silp) [4], Tohoku [5], and Pennsylvania [6,7])

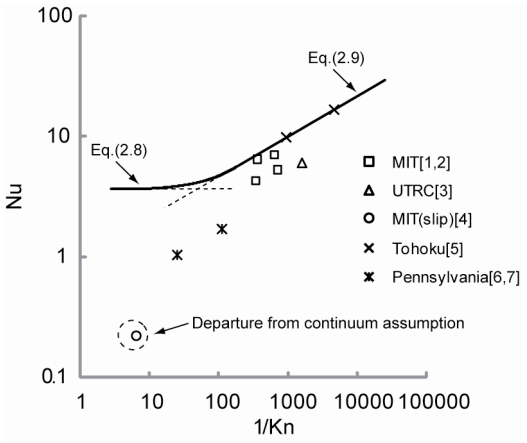

Fig.2.4 Relationship between Nu and Kn (MIT [1,2], UTRC [3], MIT (silp) [4], Tohoku [5], and Pennsylvania [6,7])

The second-order slip or higher-order Burnett equations or molecular modeling may be introduced for the transition flow region of $0.1 < Kn < 10$ [5]. Data of Pennsylvania [6,7] is in the slip flow regime and that of MIT (slip) [4] is in the transition regime. Therefore, both these data sets do not match the continuum calculations as shown in Fig. 2.4. The effects of the slip and lack of accommodation are expressed in terms of the discontinuity in temperature θ between the boundary and the gas as [9]

$$\theta = g\frac{dT}{dy} \quad , \tag{2.10}$$

where g is the coefficient for the temperature jump and is on the order of λ. Therefore, the effects of the slip and lack of accommodation minimize heat transfer at the solid wall and the experimental Nu value is smaller than the value obtained by continuum assumption, as shown in Fig.2.4.

Equation (2.7) indicates Nu and heat transfer film coefficient scale as a power function of d_H,

$$Nu \propto Re^{1/3} \propto {d_H}^{1/3} \quad , \tag{2.11}$$

$$h = \frac{k \cdot Nu}{D_H} \propto {d_H}^{-2/3} , \tag{2.12}$$

where k is the thermal conductivity. The scaling law of the heat transfer described by Eq. (2.12) corresponds to the case of $m = 2/3$ in Eq. (2.6). From the obtained map for the operation envelope of microscale nozzle flow, our microscale nozzle was designed with the values of $Kn < 10^{-3}$ and $Nu \cong 15$ that form a continuum flow region

2.2 Geometrical Design of Convergent-Divergent Microscale Nozzle

The method of characteristics [9,11] with weak waves was applied to the design of the divergent section of the microscale nozzle. The problem in this method is that the flow should be expanded from $M = 1$ at the throat to $M = 1.366$ in the discharge section. The throat area is chosen as 100μm x 300μm to choke the mass flow rate of $\dot{m} = 0.02 g/sec$. We have chosen the Prandtl–Meyer function [9,11] as $\nu(M) = 8$, which corresponds to $M = 1.366$. The brief design steps are as follows.

(1) The initial expansion is divided into four segments with the same deflection angle of 1°. Thus, the corresponding maximum value of the wall deflection is $\theta_{max} = 4^\circ$.
(2) The waves are reflected from the centerline of the symmetrical nozzle configuration.
(3) In the section of cancellation, the reflected waves are cancelled by deflecting the wall 1° at each wave intersection.
(4) The discharge section height must agree with the value of $A_3/A^* = 1.14$ that corresponds to $\nu(M) = 8$.

Figure 2.5 depicts the divergent section of the microscale nozzle contour. The local Re increases from 5×10^3 at the throat to 7×10^3 in the discharge section. The transition Re of the laminar boundary layer for a flat plate ranges from 5×10^5 to 5×10^6 [14]. Therefore, we apply the laminar boundary layer model for a flat plate to the nozzle wall section to compensate the effective cross-sectional area for nozzle flow. The plate boundary layer displacement can be expressed as [14]

$$\delta_D = 1.721\sqrt{\frac{\nu x'}{u^\infty}}, \tag{2.13}$$

where u^∞ is the core flow velocity, ν is the kinetic viscosity, and x' is the distance from the throat along the solid wall. The cross-sectional area of discharge to the throat was found to be $A_3/A^* = 1.14$ on the basis of Eq. (2.13).

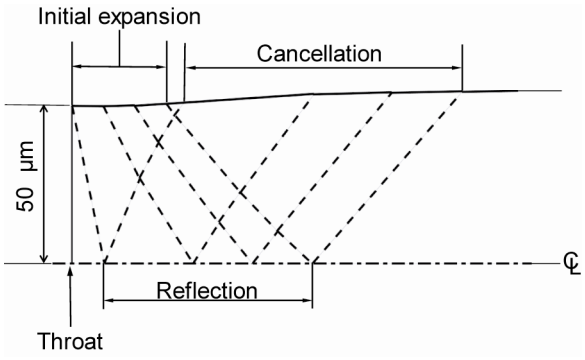

Fig.2.5 Divergent section of microscale nozzle contour on the basis of method of the characteristics

2.3 Microfabrication

In this section, the microfabrication process for a device for a direct wall static pressure measurement of nozzle flow is described. Figures 2.6(a) and 2.6(b) show the exposed schematic views of the device structures observed from the front and back sides, respectively. The microscale nozzle throat in the device has a width of 100μm and a height of 300μm. The external dimensions of the device are 20mm x 20mm x 2mm. The device is composed of three microfabricated layers. Layer #1 is a 1mm thick SD2 Pyrex glass (Hoya Candeo Optronics) and layers #2 and #3 are 500-μm thick n-type single-crystal silicon (Si) wafers. We chose the Pyrex glass as layer #1 for ease in micromilling, compatibility for bonding with Si, and flow visualization during the experiment. The front side of layer #2 forms the convergent and divergent channels of nozzle flow, two buffer tanks and two Pitot tubes that are located upstream and downstream of nozzle flow (Fig.2.6(a)). In contrast, the back side of layer #2 forms pressure channels that can lead static pressures from wall taps and total pressures from Pitot tubes to layer #3 via trench holes (Fig.2.6(b)). The layout of pressure channels on the back side of layer #2 is extended from the center to radial outward directions (Figs.2.6(b), 2.8(b), and 2.9(b)). This configuration allows us to connect the small-scale device to a mechanically machined plastic interface. The material of the plastic interface is polymethylmethacrylate (PMMA).

The Si microstructures of layers #2 and #3 described above (i.e., nozzle flow channels, buffer tanks, Pitot tubes, and trench holes) are fabricated by the silicon bulk micromachining technology. Both sides of the Si microstructures are patterned by ultraviolet (UV) lithography. The image reversal photoresist AZ5214E (Clariant Corporation), which is suitable for a lift-off process, is used for UV lithography. After patterning the photoresist on the Si substrate, the Cr mask used for a dry etching process is formed by vacuum vapor deposition and lift-off processes. Both sides of the Si microstructures are etched using an inductively coupled

plasma-reactive ion etching (ICP-RIE) instrument (Multiplex ASE-SRE; Surface Technology Systems—Sumitomo Precision Products). The typical etching conditions used are a 150 SCCM SF_6 flow rate for a 7.5 s cycle, a 22W platen power, and a 600W coil power, followed by a 100 SCCM C_4F_8 flow rate for a 5.0 s cycle, no platen power and a 600W coil power (SCCM denotes cubic centimeters per minute at standard temperature and pressure). After the ICP-RIE of the microstructures in layer #2, the static pressure taps of a 5-μm diameter circular opening with a 200μm hole length, which are located along the basal wall from the throat toward the downstream direction of nozzle flow (Figs.2.7(a) and 2.7(b)), are formed using a focused ion beam (FIB) instrument (FB2200; Hitachi High Technology Corporation). To investigate the influence of geometrical dimensions of the pressure taps on flow in nozzle, 5-μm, 10-μm, and 30-μm diameter circular openings were examined for a preliminary experiment. The experimental values of the static pressures were varied with the variation in diameters of the pressure taps.

However, in the case of 5-μm and 10μm-diameter circular openings, experimental values of the static pressures were saturated and independent of the geometrical dimensions. Therefore, we adopt a 5-μm-diameter circular opening, which is possibly the smallest dimension with the current FIB process for a final experiment (see footnote 1).

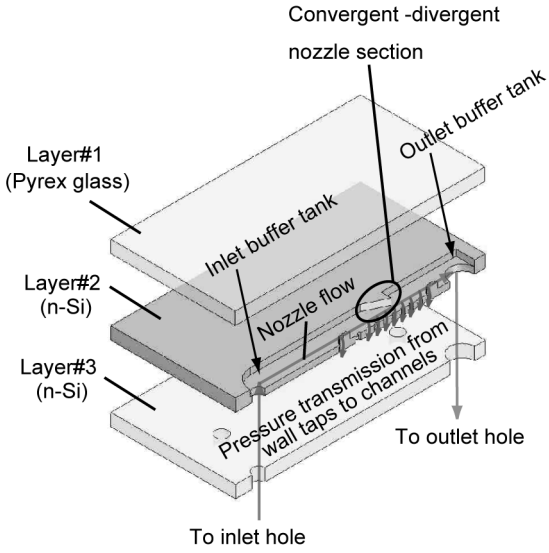

(a)

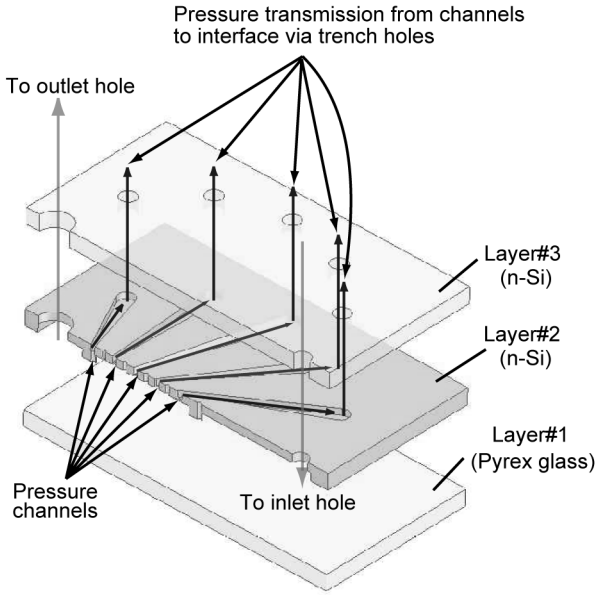

(b)

Fig.2.6 Exposed schematic views of device structures observed from front (a) and back (b) sides

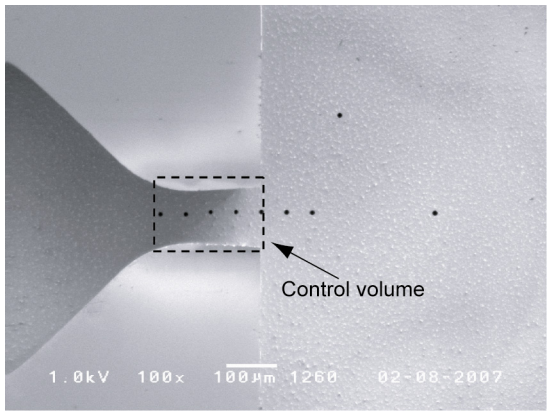

(a)

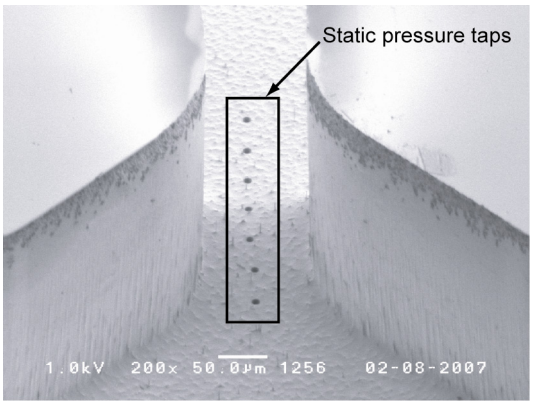

(b)

Fig.2.7 Scanning electron microscope images of exposed view of nozzle and wall static pressure taps. (a) Convergent-divergent nozzle section and (b) Exposed view of throat from downstream to upstream.

Finally, each layer is aligned and bonded together to form a multilayer nozzle assembly. Anodic bonding is applied to bond layers #1 and #2. In contrast, eutectic bonding is applied to layers #2 and #3. Reference [15] indicates a similar wafer bonding process in the fabrication of multilayer silicon microstructures.

Appropriate etching conditions for minimizing the undercut (lateral) etching of the microstructures of the nozzle channels, buffer tanks, Pitot tubes and trench holes, and the dark regions composed of microscale masked silicon pillars were determined by preliminary experiments. These are important geometrical issues that may affect the aerodynamic performance due to the variation in effective cross-sectional area.

The Pitot tubes and the static pressure taps were fabricated by the batch processes of UV lithography and silicon deep trench etching. The width and height of the Pitot tube are approximately 50μm and 300μm, respectively (aspect ratio of 6). However, an aspect ratio of 6 may be a critical dimension, which has been able to materialize using the current level of the silicon bulk micromachining technology.

Figure 2.7(a) shows a scanning electron microscope (SEM) image of the exposed view of the nozzle and wall static pressure taps observed from the front side of the device. In Fig.2.7(a), an area enclosed by a dotted line corresponds to the area from the throat to the exit. Figure 2.7(b) shows a SEM image of the exposed view of the nozzle and wall static pressure taps observed from the downstream direction to the upstream direction. Figsures 2.8(a)–2.8(d) show the photomicrographs of the front and back sides of layer #2, the back side of layer #3, and an exposed view of the completely assembled device, respectively.

Foot note 1:

To support the above-mentioned experimental evidence, CFD analysis (CFX ver. 6.1) was carried out for the flow field around the pressure tap. If a secondary flow, which disturbs the main core flow field parallel to the channel wall, is induced at vicinity of the pressure tap, the pressure gradient normal to the wall ∇p is generated. The nozzle has favorable density (pressure) gradient $\nabla \rho$ along the divergent channel section. Therefore, span-wise vortex $\boldsymbol{\omega}$ is generated at the inlet region of the pressure tap due to the vorticity equation, i.e., $D\boldsymbol{\omega}/Dt \propto \nabla\rho \times \nabla p$ [16]. Indeed, the span-wise vortex was generated at 10-μm, 20-μm and 30-μm-diameters but disappeared at a 5-μm-diameter.

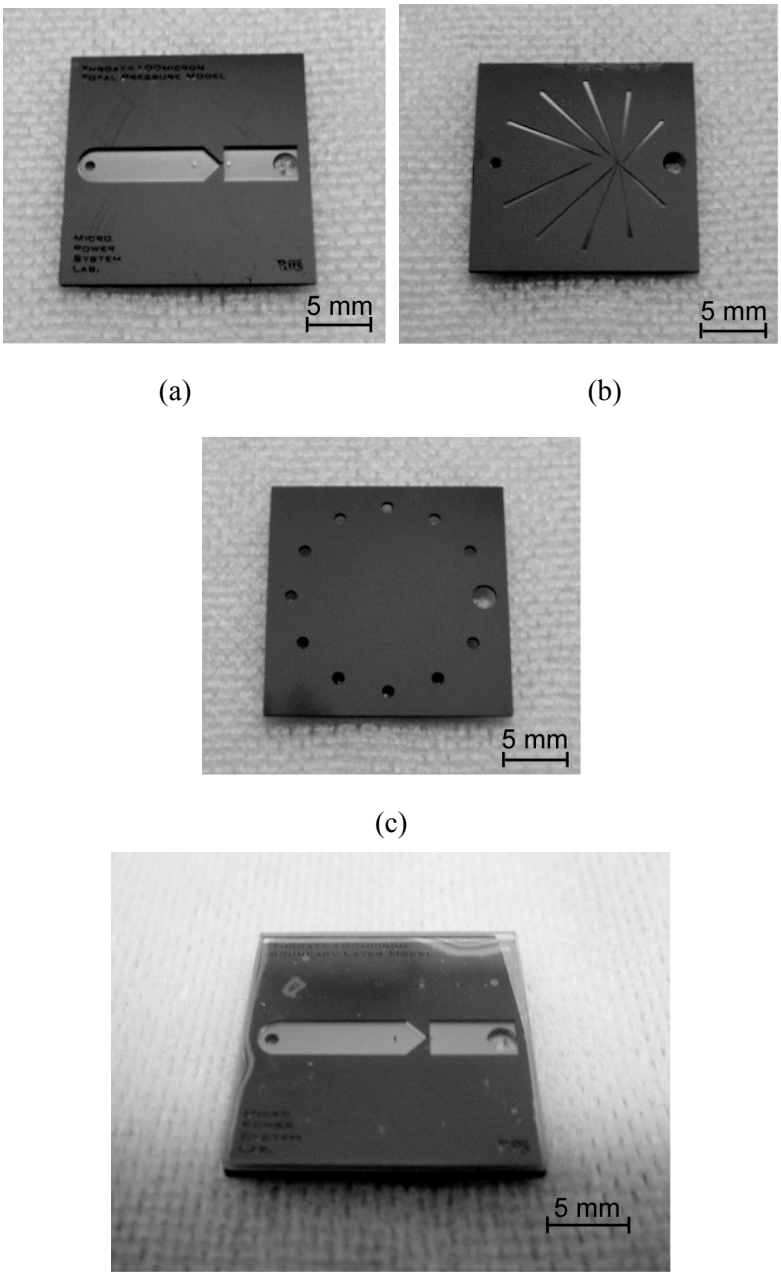

(a) (b)

(c)

(d)

Fig.2.8 Photomicrographs of fabricated device. (a) Layer #2 (front side), (b) layer #2 (back side), (c) layer #3, and (d) assembled multilayer structure.

2.4 Experimental Procedure

Two buffer tanks are located upstream and downstream of nozzle flow. These are used to maintain the stagnation state of the working fluid. The dry air (29% O_2 and 81% N_2) used as the working fluid is supplied from the inlet hole of the 1mm diameter circular opening of the upstream buffer tank and discharged throughout the nozzle from the outlet hole of the 2mm diameter circular opening of the downstream buffer tank. Total and static pressures, which are extracted from the Pitot tubes and the wall static pressure taps, are led to the pressure channels located on the back side of the device. Such pressures are continuously transmitted from the pressure channels to the trench holes of the device, in order to lead them to the interface for pressure measurement. The interface connects the small-scale device to a large-scale external feed system, which includes pressure sensors and gas-inlet and discharge lines. Pressures are measured using pressure sensors (AP-43 and AP-44; Keyence). Mechanical seals are concentrically located between the interface and the device to prevent fluid leakage. This structure confirms the transmission of fluid from the interface to the device without leakage and vice versa. For pressure measurement, the device is fixed by the top and bottom interfaces, as shown in Fig.2.9(a). As previously mentioned, the mechanical seals are located between the device and the bottom interface, as shown in Fig.2.9(b). The inlet and outlet ports are connected to the external gas feed system and located on the lower part of the bottom interface. Figure 2.10 shows the schematic view of the experimental setup for pressure measurement. The pressure sensors and mass flow meter for flow control are located upstream and downstream of the interface. The pressure sensors used for direct wall static pressure measurements are located at the surrounding stations of the device, as shown in Fig.2.9(a). On the other hand, the pressure sensors used for total pressure measurements are located at the inlet and outlet buffer tanks.

The downstream discharge tank was opened to an atmospheric pressure of 101.3 kPa and kept at a room temperature of 298 K. To estimate the preliminary inlet stagnation pressure, a one-dimensional isentropic flow throughout the nozzle was assumed [10,11],

$$\frac{p_0}{p} = \left(1 + \frac{\gamma - 1}{2} M^2\right)^{\gamma/(\gamma-1)} \quad . \tag{2.14}$$

The design values of $M = 1.366$ and P=101.3kPa in the discharge section were substituted into Eq. (2.14) to obtain the preliminary inlet stagnation pressure of P_0=307kPa.

2.5 Experimental Results and Discussion

Figure 2.11 shows the result of the direct measurement of the static pressure distribution along the divergent section of the nozzle wall. Before performing any experiment, a gas leakage

from the experimental set up was investigated. The gauge pressures from 100 to 200 kPa with a 50 kPa step increment were applied to the upstream inlet port of the microscale nozzle while the downstream discharge port was completely closed. We confirmed that each pressure sensor connected to the microscale nozzle indicates the same value to the applied gas pressure. Any gas leakage from the experimental set up was not observed. Therefore, the full-scale linearity of each pressure sensor has the highest contribution to the total experimental uncertainty of the static pressure distribution depicted in Fig.2.11. Figure 2.12 shows a comparison of the solution for one-dimensional isentropic nozzle flow [10,11], and the experimental data obtained by the authors and other institutions. The experimental values of p_0/p against the arbitrary values of A^*/A are different from the solution of isentropic nozzle flow expressed as

$$A^*/A = \left\{ \left[1 - \left(\frac{P_0}{P} \right)^{\frac{1-\gamma}{\gamma}} \right]^{\frac{1}{2}} \left(\frac{P_0}{P} \right)^{-\left(\frac{1}{\gamma}\right)} \right\} \Bigg/ \left[\left(\frac{\gamma-1}{2} \right)^{\frac{1}{2}} \left(\frac{2}{\gamma+1} \right)^{\frac{\gamma+1}{2(\gamma-1)}} \right] \quad [10,11].$$

This experimental evidence suggests that the static pressure distribution of microscale nozzle flow does not appear to follow the isentropic flow assumption. The reason why the isentropic flow assumption failed will be discussed in Sec. 2.5.1.

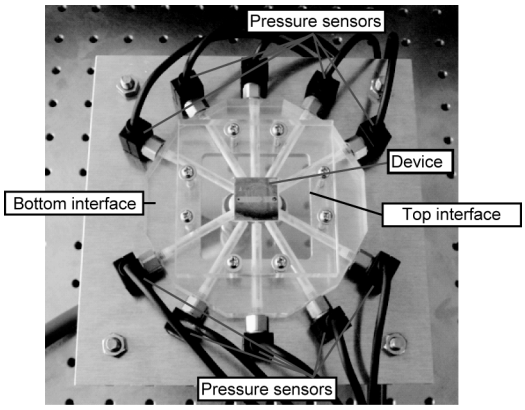

(a)

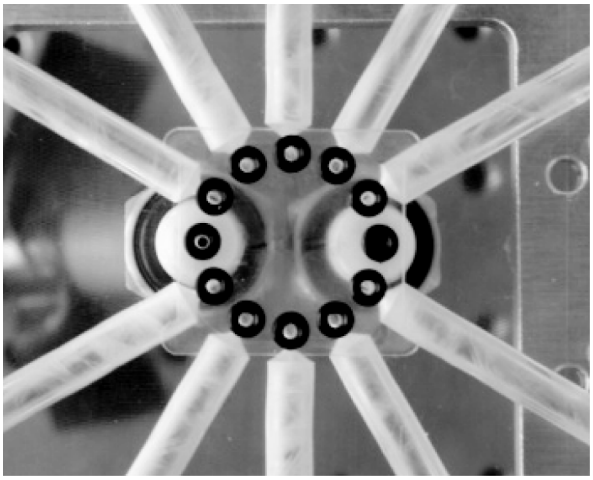

(b)

Fig.2.9 Schematic views of device fixture for pressure measurement. (a) Device fixed to interface and (b) configuration of mechanical seals.

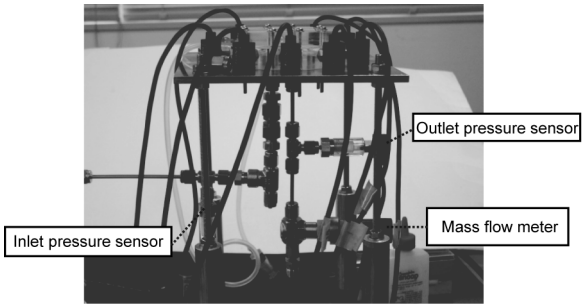

Fig.2.10 Schematic view of experimental setup for pressure measurement

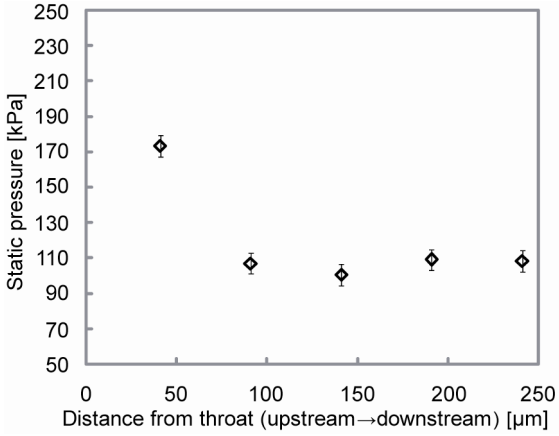

Fig.2.11 Result of direct measurement of static pressure distribution along divergent section of nozzle wall

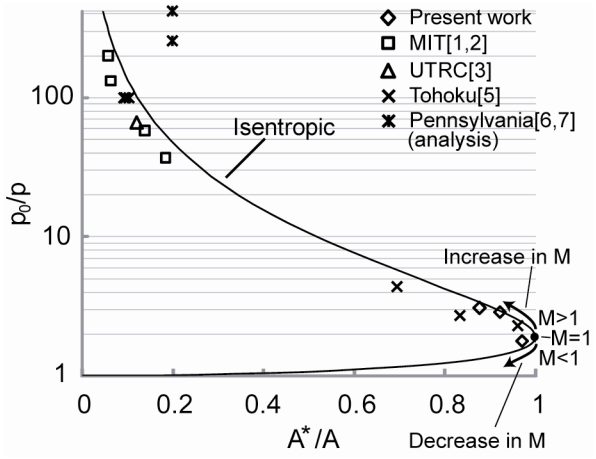

Fig.2.12 Comparison of solution for one-dimensional isentropic nozzle flow and experimental data obtained by the authors and other research institutions (MIT [1,2], UTRC [3], Tohoku [5], and Pennsylvania [6,7])

2.5.1 Differential Equation for Continuum Nonisentropic Nozzle Flow

The one-dimensional analysis of continuum compressible flow can be carried out by the application of the Reynolds transport theorem to the conservation equations for the elementary control volume shown in Fig.2.13. As pointed out by Shapiro, the influence coefficients for the change in Mach number throughout the nozzle flow can be expressed as [10,11]

$$dM^2 = F_A \frac{dA}{A} + F_{T_0} \frac{dT_0}{T_0} + 4C_f F_{cf} \frac{dx}{d_H}, \tag{2.15}$$

where $F_A = -\dfrac{2M^2\left(1+\dfrac{\gamma-1}{2}M^2\right)}{1-M^2}$, $F_{T_0} = \dfrac{M^2\left(1+\gamma M^2\right)\left(1+\dfrac{\gamma-1}{2}M^2\right)}{1-M^2}$, and $F_{cf} = \dfrac{\gamma M^4\left(1+\dfrac{\gamma-1}{2}M^2\right)}{1-M^2}$.

The influence coefficients F_A, F_{T_0} and F_{cf} are the partial derivatives of dM^2 with respect to dA/A, dT_0/T_0 and dx/d_H, respectively.

The influence coefficients express the effects of the cross-sectional area change, the adiabatic flow with friction, and the nonadiabatic flow with wall heat transfer on the so-called nonisentropic nozzle flow.

The recovery factor (R) is defined as [9,10,14,16]

$$R \equiv \frac{\dfrac{T_{aw}}{T} - 1}{\dfrac{\gamma-1}{2}M_\infty{}^2}, \tag{2.16}$$

where T is the static temperature of core flow, and T_{aw} is the adiabatic wall temperature (Fig.2.14).

To apply the Reynolds analogy to the nonisentropic nozzle flow calculation, we define the energy conservation equation as [10,16]

$$\dot{m}dQ = \frac{\pi}{4} d_H{}^2 \rho u C_p dT_0 = h\pi d_H dx\left(T_w - T_{aw}\right), \tag{2.17}$$

where d_H is the hydraulic diameter, T_w is the solid wall temperature, and dx is the infinitesimal distance along the wall. The combination of Eqs. (2.16) and (2.17) leads to the elimination of the adiabatic wall temperature,

$$\frac{dT_0}{T_w - T\left(1+R\frac{\gamma-1}{2}M^2\right)} = \frac{4h}{\rho u C_p}\frac{dx}{d_H}. \tag{2.18}$$

The relationship between the derivatives of stagnation and static temperatures in the nonadiabatic Rayleigh flow was derived by Zukoski [17],

$$dT_0 = \left(\frac{1-M^2}{1-\gamma M^2}\right)dT. \tag{2.19}$$

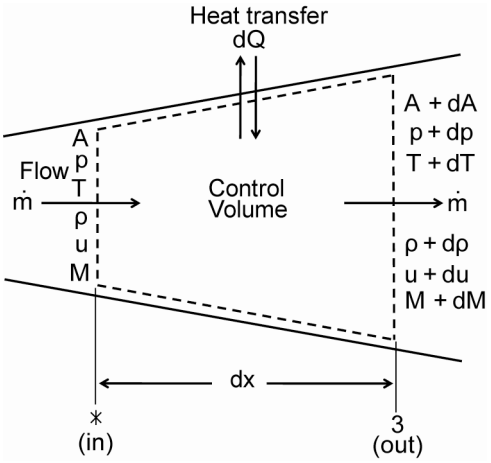

Fig.2.13 Definition of elementary control volume

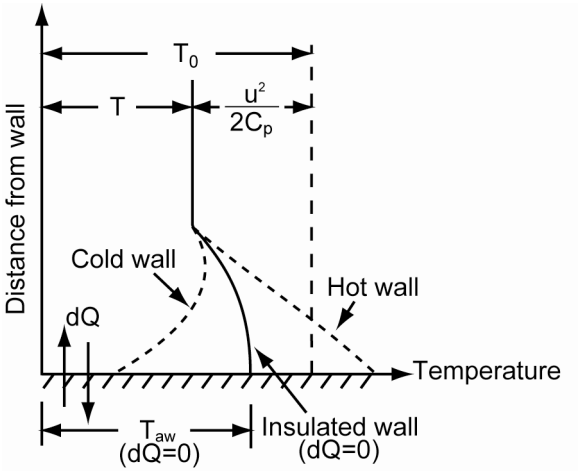

Fig.2.14 Basic concept of recovery factor

Substituting Eq. (2.19) into Eq. (2.18), we obtain

$$\frac{dT}{T_w - T\left(1+R\frac{\gamma-1}{2}M^2\right)}\left(\frac{1-M^2}{1-\gamma M^2}\right) = \frac{4h}{\rho u C_p}\frac{dx}{d_H}. \tag{2.20}$$

The Reynolds analogy, which is valid for fluid with $Pr \neq 1$, was derived by Colburn as [14,16,18,19] (see footnote 2)

$$\frac{h}{\rho u C_p} Pr^{2/3} = \frac{C_f}{2}. \tag{2.21}$$

Thus, Eq. (2.20) can be rewritten as

$$\frac{dT}{T_w - T\left(1+R\frac{\gamma-1}{2}M^2\right)}\left(\frac{1-M^2}{1-\gamma M^2}\right)Pr^{2/3} = 2C_f\frac{dx}{d_H}. \tag{2.22}$$

Substituting Eqs. (2.19) and (2.22) into the right-hand terms of Eq.(2.15), we obtain an original differential equation that can be used to solve our problem, which takes into account the cross-sectional area change, the adiabatic flow with friction, and the nonadiabatic flow with wall heat transfer,

$$dM^2 = F_A\frac{dA}{A} + \frac{M^2\left(1+\gamma M^2\right)}{1-\gamma M^2}\frac{dT}{T} + \frac{2TF_{cf}\,Pr^{2/3}}{T_w - T\left(1+R\frac{\gamma-1}{2}M^2\right)}\left(\frac{1-M^2}{1-\gamma M^2}\right)\frac{dT}{T}. \tag{2.23}$$

Schlichting and Gersten derived the recovery factor for the flat plate boundary layer [14],

$$R \cong \frac{\kappa}{\kappa_\theta}\left[1+1.2\sqrt{\frac{Cf}{2}} + O\left(\frac{Cf}{2}\right)\right], \tag{2.24}$$

where $\kappa/\kappa_\theta = 0.87$ is the Karman constant. By applying the Blasius solution of $Cf = 0.664/\sqrt{Re}$ for the laminar boundary layer [14,16] to Eq. (2.24), it can be concluded that the recovery factor scales as $R \propto 1/Re^{1/4} \propto 1/d_H{}^{1/4}$.

As mentioned in the preceding section, the local Re is as high as 7×10^3 at the discharge

section. Thus, the recovery factor with $Cf = 0.664/\sqrt{Re}$ is found to be $R \cong 0.9$ in our case. Therefore, heat dissipation in the microscale boundary layer enhances following the scaling law, i.e., $R \propto 1/d_H{}^{1/4}$. In contrast, the solution of the Falkner–Skan similarity equation of $R = \sqrt{Pr} \cong 0.8$ [16], which is free from scaling, is usually used for large-scale nozzles. The pressure gradient normal to the channel wall (y-direction) can be expressed as $\partial p/\partial y \approx \rho u^2/R_C$, where R_C is a radius of the curvature of the wall. The integration is carried out for this form assuming a linear velocity distribution, i.e., $u = u^\infty y/\delta$, where u^∞ is the core flow velocity and δ is the boundary layer thickness. We obtain the equation as $p(\delta) - p(0) \approx \rho u^2 \delta/3R_C$. If $R_C >> \delta$, this term is negligibly small. The present work satisfies this condition, and the flat plate boundary-layer solution is still valid for our application. The numerical integration of Eq. (2.23) leads to the variation in Mach number with respect to the cross-sectional area change, friction, and wall heat transfer. The static pressure change throughout the control volume can be derived by the combination of the solutions of Eq. (2.23) and the local fluid state equation as [11]

$$\frac{p_{out}}{p_{in}} = \frac{M_{in}}{M_{out}} \sqrt{\frac{T_{out}}{T_{in}}} \frac{A_{in}}{A_{out}} . \tag{2.25}$$

We define the control volume as the enclosed region shown in Fig.2.7(a). Figure 2.15 shows a comparison of the experimental results and the calculations based on Eqs. (2.23) and (2.25). As can be seen from the figure, throughout the divergent section of the throat downstream, Shapiro's nonisentropic flow concept interprets the experimental evidence that the empirical static pressure is higher than that obtained by isentropic flow calculation. Therefore, the effects of friction and heat transfer play an important role in aerodynamic design in the microscale region. The width and height of the Pitot tubes are relatively smaller than that of the upstream and downstream geometrical dimensions of the channel (mm-scale) where the Pitot tubes are located.

Footnote 2:

Indeed, $\frac{h}{\rho u C_p} Pr^{2/3} F(\beta) = \frac{C_f}{2}$ holds for Falkner–Skan-type flow [14,16]. The factor $F(\beta)$ is a measure of the pressure gradient. If $\beta > 0$, the pressure gradientis negative or favorable. Naturally, $\beta = 0$ and $F(0) = 1$ denote a flat plate. $0 < \beta << 1$ and $F(\beta) \cong 1$ hold for our nozzle flow. This corresponds to the modest pressure gradient. Thus, the Reynolds analogy is reliable.

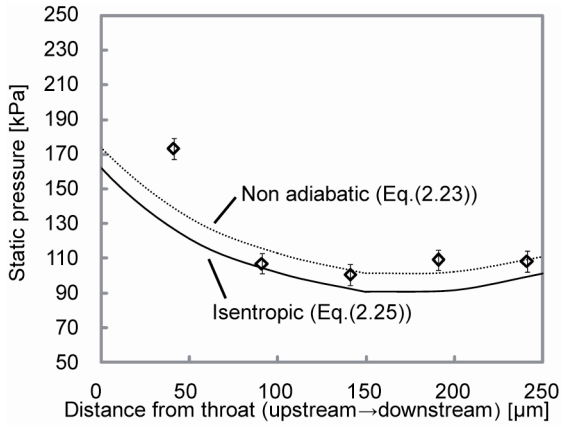

Fig.2.15 Comparison of experimental results and calculations on the basis of on Eqs. (2.23) and (2.25)

Therefore, the core flow stagnation pressure drop due to the kinetic dissipation of the local flow around the Pitot tube (profile and mixing losses) can be neglected compared to the stagnation pressure change due to the wall friction and heat transfer of the present work. To confirm the validity of our concept, we will make a comparison of the experimental results obtained by other research institutions and the calculations based on Eqs. (2.23)-(2.25). The calculation of the stagnation-to-static pressure ratio of p_0/p against the throat-to-discharge cross- sectional area ratio of A^*/A was carried out on the basis of Eqs. (2.23)-(2.25). In the calculation, the solid wall temperature of $Tw = 300K$ was assumed. Figure 2.16 shows a comparison of the calculations and the experimental results. The calculations are in good agreement with the experimental results obtained by the present work and other research institutions [1-7,20-23]. Therefore, friction and heat transfer play an important role in the reduction in stagnation-to-static pressure ratio against the arbitrary fixed value of the throat-to-discharge cross-sectional area ratio. It can be concluded that the achievable Mach number of the actual nonisentropic flow is lower than that of the ideal isentropic flow for a fixed nozzle geometry. Indeed, our experimental discharge Mach number is found to be 1.1, which is lower than the design isentropic value of 1.366. However, the result obtained by Alexeenko et al. does not appear to follow the calculation [6,7].

Their data is a solution of the direct simulation Monte Carlo (DSMC) analysis with the following boundary conditions: an inlet primary flow temperature of $2000K$ and a solid wall temperature of $Tw = 700K$. Indeed, our calculation was carried out using these boundary conditions. The discrepancy between the calculation and experimental data was still observed; however, the qualitative tendency was interpreted on the basis of the proposed concept. One possible reason for the weak correlation of the data is the strong coupling between the velocity and thermal boundary layers of high-temperature rarefied combustion gas flow. In contrast, in

our calculation, we assume continuum flow with weak coupling between the thermal and velocity fields in the boundary layer, i.e., the temperature does not affect the velocity profile in the boundary layer.

2.5.2 Shapiro's Influence Coefficients

In this section, each individual effect of the influence coefficients F_A, F_{T0} and F_{cf} on the aerodynamic performance of nozzle flow is clarified [10,11]. Figure 2.17 depicts the variations in F_A, F_{T0} and F_{cf} as a function of flow Mach number. The signs of FT0 and F_{cf} are opposite to that of F_A, and the absolute value of F_{T0} is larger than that of F_{cf} from the subsonic-to-supersonic flow region. The effect of F_A on the Mach number increment of dM^2 can be compensated by both F_{T0} and F_{cf}. Therefore, it can be considered that the achievable Mach number of the actual nonisentropic flow is lower than that of the ideal isentropic flow as mentioned in Sec. 2.5.1, and the effect of wall heat transfer plays a dominant role in the aerodynamics of nozzle flow.

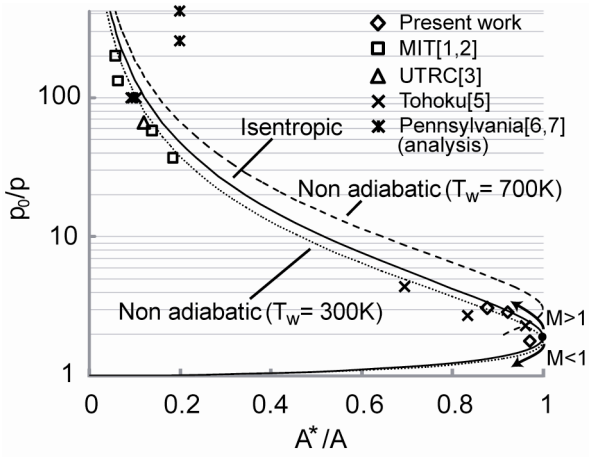

Fig.2.16 Comparison of calculations and experimental results (MIT [1,2], UTRC [3], Tohoku [5], and Pennsylvania [6,7])

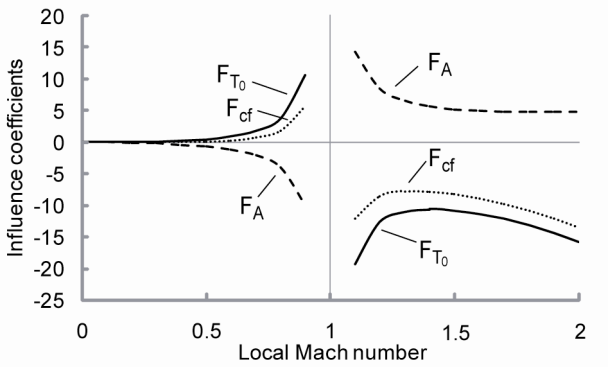

Fig.2.17 Variations in F_A, F_{T_0} and F_{cf} as a function of flow Mach number

2.6 Conclusion

A microscale supersonic nozzle was fabricated by silicon bulk micromachining technology (see Table 2.1). The operation envelope that determines whether the continuum or rarefied flow assumption is appropriate can be expressed as a function of Kn and related parameters. The effect of nonadiabatic operation on microscale nozzle flow was investigated on the basis of wall heat transfer. These physical correlations were considered for the classical Shapiro's equations to analyze the microscale nozzle flow aerodynamics. Furthermore, the solutions of the Shapiro's equations were compared with the experimental results by the authors and other research institutions, in order to demonstrate the validity of the proposed aerodynamics design concept for microscale continuum flow.

Table 2.1 Design specification of microscale supersonic nozzle

Preliminary design specification of microscale supersonic nozzle	
Nozzle depth(=Throat depth) (h)	300 μm
Throat width (L)	100 μm
Area ratio (A_3:A^*)	1.14:1
Duct length of divergent section(x)	142 μm
Inlet temperature (T_1)	300 K
Inlet total pressure (p_{01})	307 kPa
Design outlet Mach number (M_3)	1.366

References

[1] Bayt, R. L., and Breuer, K. S., 1998 "Viscous Effects in Supersonic MEMSFabricated Nozzles," Proceedings of the 1998 ASME International Mechanical Engineering Congress and Exposition, Anaheim, CA, ASME. New York, pp. 117–123.

[2] Bayt, R. L., 1999, "Analysis, Fabrication and Testing of a MEMS-Based MicropropulsionSystem," Ph.D. thesis, Department of Aeronautics and Astronautics, MIT, Cambridge, MA.

[3] Bayt, R. L., and Kenneth, S. B., 2001, "Analysis and Testing of a Silicon Intrinsic-Point Heater in a Micropropulsion Application," Sens. Actuators, A, 91, pp. 249–255.

[4] Arkilic, E. B., Schmidt, M. A., and Breuer, K. S., 1997, "Gaseous Slip Flow in Long Microchannels," J. Microelectromech. Syst., 6, pp. 167–178.

[5] Nagai, H., Naraoka, R., Sawada, K., and Asai, K., 2008, "Pressure-Sensitive Paint Measurement of Pressure Distribution in a Supersonic Micronozzle," AIAA J., 46, pp. 215–222.

[6] Alexeenko, A. A., Fedosov, D. A., Gimelshein, S. F., Levin, D. A., and Collins, R. J., 2006, "Transient Heat Transfer and Gas Flow in a MEMS-Based Thruster," J. Microelectromech. Syst., 15, pp. 181–194.

[7] Alexeenko, A. A., Levin, D. A., Fedosov, D. A., Gimelshein, S. F., and Collins, R. J., 2005, "Performance Analysis of Microthrusters Based on Coupled Thermal-Fluid Modeling and Simulation," J. Propul. Power, 21, pp. 95–101.

[8] Bird, G. A., 1994, Molecular Gas Dynamics and the Direct Simulation of Gas Flows, Oxford University, New York, Chap. 1.

[9] Liepmann, H. W., and Roshko, A., 1957, Element of Gasdynamics, Wiley, Chap. 4,5,12–14.

[10] Shapiro, A. H., 1953, The Dynamics and Thermodynamics of Compressible Fluid Flow, Ronald, New York, Chap. 7,8.

[11] Greitzer, E. M., Tan, C. S., and Graf, M. B., 2006, Internal Flow, Cambridge University, Cambridge, UK, Chap. 2,10.

[12] Graetz, L., 1883, "Über die Wärmeleitungsfähigkeit von Flüssigkeiten," Ann. Phys. Chem., 18, pp. 79–94.

[13] Sellars, J. R., Tribus, M., and Klein, J. S., 1956, "Heat Transfer to Laminar Flow in a Round Tube or Flat Conduit the Graetz Problem Extended," ASME, 78, pp. 441–448.

[14] Schlichting, H. S., and Gersten, K., 1996, Boundary Layer Theory, 8th ed., McGraw-Hill, New York, Chap. 6–9,16–18.

[15] Namura, M., and Toriyama, T., 2012, "Aero-Thermodynamic Consideration of Single-Crystal-Silicon Premixed-Fuel Microscale Can Combustor," ASME J.Eng. Gas Turbines Power, 134, p. 071501.

[16] White, F.M., 1991, Viscous Fluid Flow, 2nd ed.,McGraw-Hill, New York, Chap. 4.

[17] Zukoski, E. E., 1985, "Afterburners," Aerothermodynamics of Aircraft Engine Components, G. C. Oates, ed., American Institute of Aeronautics and Astronautics Inc., Reston, VA, Chap. 2.

[18] Knudsen, J. G., and Katz, D. L., 1958, Fluid Dynamics and Heat Transfer, McGraw-Hill, New York, Chap. 13.

[19] Bird, R. B., Stewart, W. E., and Lightfoot, E. N., 1960, Transport Phenomena, Wiley, New York, Chap. 13.

[20] Reed, B. D., de Groot, W., and Dang, L., 2001, "Experimental Evaluation of Cold Flow Micronozzles," AIAA Paper No. 2001-3521.

[21] Hitt, D. L., Zakrzwski, C. M., and Thomas, M. A., 2001, "MEMS-Based Satellite Micropropulsion via Catalyzed Hydrogen Peroxide Decomposition," Smart Mater. Struct., 10, pp. 1163–1175.

[22] Mueller, J., Chakraborty, I., Bame, D., and Tang, W., 2000, "Vaporizing Liquid Microthruster Concept. Preliminary Results of Initial Feasibility Studies," Micropropulsion for Small Spacecraft, Progress in Astronautics and Aeronautics, Vol. 187, M. Micci and A. Ketsdever, eds., AIAA, Reston, VA, pp. 215–230.

[23] London, S. A. P., Epstein, A. H., and Kerrebrock, J. L., 2001, "High-Temperature Bipropellant Microrocket Engine," J. Propul. Power, 17(4), pp.780–787.

Chapter 3

Aero-thermodynamics of Single-Crystal Silicon Microscale Can Combustor

3.1 Engineering Significance of the Burning Velocity Model

A new combustor design may be based on past experience to a large extent. A useful way in which past experience can be accumulated is through the use of diagrams. For example, combustion efficiency data from all known combustors can be plotted against all the relevant variables. Figure 3.1(a) shows such a diagram, which was first proposed by Lefebvre and Ballal [1] on the basis of the burning velocity model. The combustion efficiency can be expressed as a function of burning velocity [1],

$$\eta_c = \frac{\text{heat released in combustion}}{\text{heat available in fuel}} \propto \frac{S_u}{U_{ref}}, \tag{3.1}$$

where S_u is the burning velocity and U_{ref} is the combustor reference velocity. If U_{ref} can be expressed in terms of $\dot{m}_A, P_6$ and A_{ref}, and S_u in terms of the laminar burning velocity (see footnote 3), Eq. (3.1) becomes [1]:

$$\eta_c = f(\theta) = f\left[\frac{(P_6)^{1.75} A_{ref} (L_{ref})^{0.75} \exp(T_6/300)}{\dot{m}_A}\right], \tag{3.2}$$

where P_6 is the combustor inlet static pressure, T_6 is the combustor inlet static temperature, A_{ref} is the combustor reference area, L_{ref} is the combustor reference length and $\dot{m}_A$ is the combustor inlet mass flow rate (see footnote).

The horizontal line in Fig.3.1(a) indicates the reaction rate parameter (θ parameter) defined by the function

$$\theta \equiv \frac{(P_6)^{1.75} A_{ref} (L_{ref})^{0.75} \exp(T_6/300)}{\dot{m}_A}, \tag{3.3}$$

and the vertical line indicates the combustion efficiency. In Fig.3.1(a), enclosed areas indicate experimental data obtained from a large number of can, can-annular and annular combustors. Typical values for the combustors in modern aircraft engines [2-4] and their MEMS counterparts developed by MIT [5-8] and Singapore Institute of Manufacturing Technology (SIMTEC) [9,10] are located within the enclosed region determined by Lefebvre and Ballal [1]. The amount of experimental data as available for the combustion efficiencies of microscale combustors is extremely limited. From the viewpoint of a first approximation, however, it is expected that based on large-scale combustors and microscale counterparts obey unified physical and scaling laws based on the modified burning velocity model which accounts for the heat loss effect as follows [11,12].

In Fig.3.1(b), the theoretical overall performance curve is represented by the line drawn from the origin. As the dimensions of a combustor are reduced, according to the burning velocity model it is possible to maintain a high combustion efficiency by reducing the mass flow rate. However, the heat losses become significant with decreasing dimensions or increasing surface area to volume ratio. Thus, there are minimum dimensions below which combustion is no longer possible. The burning velocity model can be modified to account for the effect of heat losses [11,12]. This is illustrated in Fig.3.1(b) by the line drawn for prescribed dimensions falling away from the overall performance curve and intercepts the horizontal line at a finite value of θ.

The characteristic features of Fig.3.1(b) are evident in Fig.3.1(a), in which experimental results for combustion efficiency are plotted against θ. The finite value of θ and the minimum dimensions required to maintain combustion in a combustor can be obtained from Fig.3.1(a). Indeed, for any combustor, the overall performance curve includes upper and lower bands. The upper band of the performance curve shifts to the right with increasing heat losses as shown in Fig.3.1(a). This band indicates heat losses. Therefore, the burning velocity model which accounts for the heat loss effect can be represented by the minimum value of the chamber dimensions required to maintain combustion.

For critical microscale combustor design, the selection of the right boundary value of the performance curve (the upper band for θ) is recommended to account for the strong heat loss effect due to the large surface area to volume ratio.

Appropriate values of A_{ref} and L_{ref} can be obtained from Fig.3.1(a) by reading off the value of θ at the point along the horizontal axis within the enclosed area at the required combustion

efficiency. Then, the values of A_{ref} and L_{ref} can be obtained by substituting the values of P_6, T_6 and $\dot{m}_A$ corresponding to the required engine specifications into the θ parameter.

According to the experimental data obtained from MIT and SIMTEC microscale annular combustors, typical values of the combustion efficiency under ambient pressure are distributed from 40% to 90% [5-10]. Therefore, a conservative target of the combustion efficiency of 70% is selected for our combustor design. Unfortunately, the amount of quantitative data for the heat losses of microscale combustors is extremely limited. In this work, θ is selected as a parameter which corresponds to the midpoint between the upper and lower bands for the performance curve corresponding to the target combustion efficiency (η_c = 70%).

The burning velocity model, which is based on semi-empirical correlations obtained from past works is very useful for giving some physical insight into combustor design, and the validity of this concept will be demonstrated in the following sections. Once the values of the combustion efficiency, P_6, T_6 and $\dot{m}_A$ corresponding to the required design specifications are selected, the geometrical product of A_{ref} and L_{ref}, i.e., $A_{ref}(L_{ref})^{0.75}$, can be determined from Eq. (3.3). Therefore, in Sec.3.2, each value of A_{ref} and L_{ref} will be determined separately by combining the value of θ and the flame height calculated from the laminar burning velocity and laminar flame sheet thickness.

Footnote 3:

In the estimation of Re on the basis of the burning velocity for the microscale combustor, we used the laminar burning velocity in Eq. (3.1). In the burning velocity model, the effect of the turbulence velocity S_T on the combustion efficiency may be represented as a function of the laminar burning velocity S_L multiplied by the a power of Re (i.e., $S_T \propto S_L Re^a$) [11,12]. This concept was first proposed by Damköhler (NACA TM 1112, 1947). Re is also a function of the pressure loss in the chamber. For practical applications, however, the pressure loss related to Re^a is expected to be small and can be neglected. Therefore, we can estimate S_T as a function of pressure, i.e., $S_T \propto S_L \propto P_6^{(n-2)/2}$ (n is the order of the reaction) in Eq. (3.2). For further details, please refer to the original papers, Refs. [11, 12].

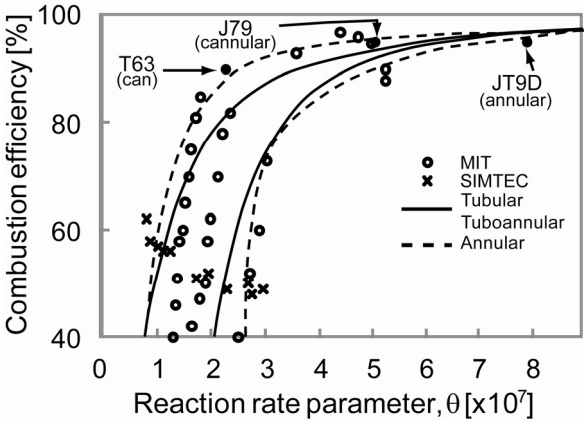

(a)

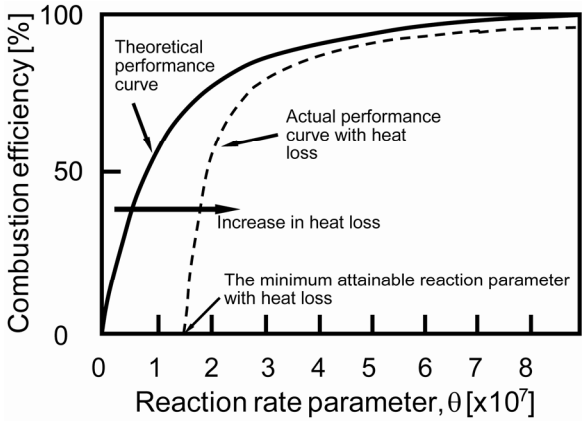

(b)

Fig.3.1 Design chart for combustion efficiencies against relevant variables on the basis of burning velocity model ($\theta \equiv \frac{(P_6)^{1.75} A_{ref} (L_{ref})^{0.75} \exp(T_6/300)}{\dot{m}_A}$) [1]

3.2 Aero-thermodynamic Design of Combustion Chamber

A combustion chamber can be divided into two zones, i.e., a flameholder wake as a primary zone and a flame propagation zone. The flameholder wake zone can be subdivided into a recirculation zone and a mixing zone. In Sec.3.2, the recirculation and flame propagation zones are used to determine the chamber dimensions. The mixing-zone concept will be used to determine the blowoff or flame extinction criteria in Sec.3.5.

3.2.1 Recirculation Zone of Flameholder Wake Flow

The general expression for the rate of entrainment of a fresh mixture into a baffle wake region is [1]

$$\dot{m}_E \equiv k\frac{\dot{m}_A}{1-B_g}, \tag{3.4}$$

where $\dot{m}_E$ is the mass flow rate of the entrainment of a fresh mixture into the baffle wake region, k is the bluff body shape factor and B_g is the blockage ratio. The coefficient k depends on the geometrical configuration of the flameholder. The measurements by Wright [13] and Zukowski [14] for 30 deg-wedge, 90 deg-flatplate and straight-hole flameholders suggest that the coefficient k for a 30 deg-wedge flameholder is also valid for 90 deg-flat-plate and straight-hole flameholders when $B_g >\sim 0.1$. The flameholder is fabricated by silicon bulk micromachining of deep straight trench microstructures formed by inductively coupled plasmareactive ion etching (ICP-RIE). Thus, multiple 90 deg-straighthole flameholder configurations are compatible with the microfabrication method.

Figure 3.2 shows the change in the geometrical boundary of the recirculation zone for the 90 deg-straight-hole flameholder with the variation of B_g. In the figure, d, x and r are the half-width of the baffle and the axial and radial distances from the baffle, respectively. This figure was drawn using Eq. (3.4) with the coefficient k for the 30 deg-wedge flameholder. As can be seen from the figure, an increase in B_g reduces the scale of the recirculation region. As mentioned in the introduction, Spadaccini et al. [8] suggested that a large recirculation zone in the flameholder wake flow reduces the effective volume of the combustion chamber. A large recirculation zone results in decreased residence time and Da. Therefore, $B_g = 0.54$ was selected to reduce the scale of the recirculation zone relative to the effective volume of the combustion chamber. From Fig.3.2, the corresponding axial spatial length of the recirculation region in the flat-hole flameholder wake flow was found to be $L = 1.2d \cong 0.1\text{mm}$, where L is the baffle wake length and d is the half-width of the bluff body. The volume of the recirculation zone was found to be $11.4\times10^{-9}\left(\text{m}^3\right)$, and does not affect the effective volume of the combustion chamber ($V_{chamber} = 277\times10^{-9}\left(\text{m}^3\right)$ in Table 3.1).

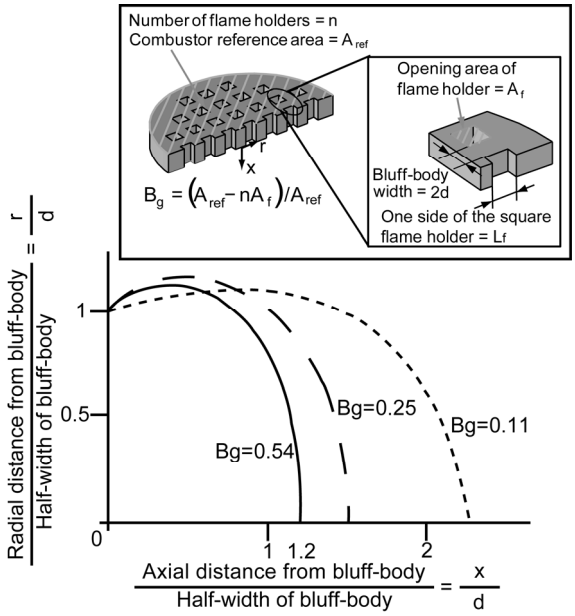

Fig.3.2 Variation of geometrical boundary of recirculation zone for straight-hole flame holder

Table 3.1 Design specifications for microscale can combustor

Micro scale can combustor	
Length (L_{ref})	1.8×10^{-3} m
Volume ($V_{chamber}$)	277×10^{-9} m^3
Cross-sectional area (A_{ref})	25.2×10^{-6} m^2
Inlet pressure (P_6)	101.3 kPa
Inlet temperature (T_6)	288 K
Mass flow rate ($\dot{m}_A$)	0.2×10^{-3} kg/s
Pressure loss ($\Delta P_0/P_0$)	≤ 5 %
Efficiency (η_c)	≥ 70 %
Exit temperature (T_g)	1300 K

3.2.2 Flame Propagation Zone

As a first approximation for the process of flame propagation, it is convenient to calculate the process of heat addition for a steady one-dimensional channel flow. The calculation is carried out for the control volume of the flame propagation zone, i.e., a flame sheet after the recirculation zone to estimate the burned gas velocity u_5 and chamber height L_{ref} as a function of u_5 (Fig.3.3). The flow process can be expressed by the differential forms of the laws of continuity, momentum and energy transport [15],

$$d(\rho u) = 0 \tag{3.5}$$

$$(\rho u)du + dp = 0 \tag{3.6}$$

$$C_p dT + udu = dh = C_p dT_t . \tag{3.7}$$

The equation for heat addition in a constant-area channel flow is an appropriate assumption for the flame propagation zone because no divergent or convergent section exists in the combustion chamber. Equations (3.5) to (3.7) can be integrated to give the change in the velocity across the heat addition zone, i.e., the flame sheet,

$$u_5 = \left(\frac{1+\gamma M_4^{\,2}}{1+\gamma M_5^{\,2}}\right)\left(\frac{M_5}{M_4}\right)^2 u_4 . \tag{3.8}$$

Equation (3.8) implies that an unburned gas with subsonic approaching velocity u_4 is accelerated to u_5 by the heat added by the flame sheet with the control volume. The flame height may be defined by the axial length required in the flame propagation zone for adjacent flames to come in contact with each other and start to coalesce. An unburned gas with velocity u_4 approaching the flame front makes a small angle of $\alpha = \sin^{-1}(S_u / u_5)$ with the flame front, where S_u is the burning velocity.

The flame height can be calculated from the combustion velocity and flame sheet thickness. From the simple geometrical consideration depicted in Fig.3.3, the flame height L_s can be determined as

$$L_S = (H / tan\,\alpha) + (\delta_L / cos(\pi/2 - \alpha)), \tag{3.9}$$

where H is the flameholder width and δ_L is the flame sheet thickness.

The channel length is directly proportional to H. Therefore, in the case of a fixed frontal inlet flow area for the flameholder A_{ref}, multiple flameholder configurations are valid for reducing the chamber length, as long as the flameholders are not too small to stabilize the combustion flame [3,4,14]. Therefore, we adopt multiple flameholder configurations, which can also be fabricated by silicon bulk micromachining.

As mentioned in the introduction, Spadaccini et al. [8] suggested that a large recirculation region in the flameholder wake flow reduces the residence time and Damköhler number and induces blowoff or flame extinction. The axial length of the recirculation zone in the flat-hole flameholder wake flow is much smaller than the flame height, i.e., $L << H/\tan\alpha$ ($L \cong 0.1\text{mm}$ as determined in Sec.3.2.1). Therefore, the condition $L << H/\tan\alpha$ may be compatible their suggestion. Finally, the approximate chamber height L_{ref} is found to be

$$L_{ref} \cong (H/\tan\alpha) + (\delta_L/\cos(\pi/2-\alpha)) \quad (3.10)$$

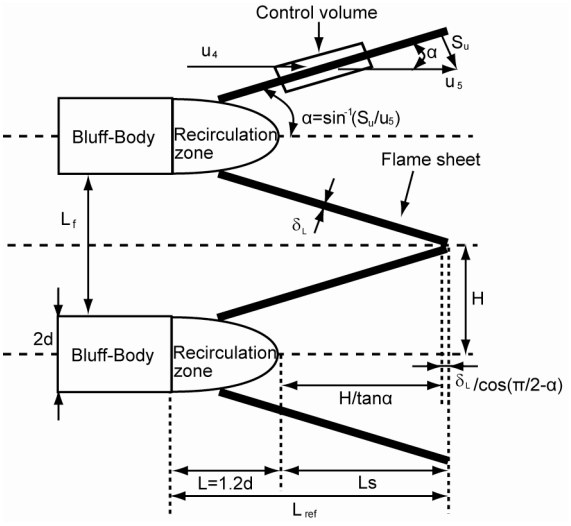

Fig.3.3 Geometrical structure of combustion flame and definition of control volume for calculation of Eqs. (3.5) to (3.8) (highly simplified)

3.2.3 Determination of Dimensions of Combustion Chamber

As mentioned in Sec.3.1, the combustion efficiency η_c (in this case η_c = 70%) must be specified before carrying out the calculation of h which accounts for the heat loss. Once the value of θ, which corresponds to the midpoint between the upper and lower bands of the performance curve shown in Fig.3.1(a), is specified to be 2×10^7, the product $A_{ref}(L_{ref})^{0.75}$ can be determined from Eq. (3.3) by the substitution of P_6, T_6 and $\dot{m}_A$. The values of P_6, T_6 and $\dot{m}_A$ are the required combustor inlet state quantities based on the Brayton cycle. However, each value of A_{ref} and L_{ref} should be determined separately to specify the dimensions of the combustor. This can be done by combining $A_{ref}(L_{ref})^{0.75}$ and L_{ref}, which are determined from Eqs. (3.3) and (3.10), respectively. Finally, the chamber volume is found to be $V_{chamber} = A_{ref}L_{ref}$. Table 3.1 summarizes the specified design parameters for the microscale can combustor.

3.2.4 Well-Stirred Reactor (WSR) Model for Combustor

The residence time in conventional gas turbine combustors is not driven primarily by the reaction rate. It is governed by the requirements for fuel-air mixing and the dilution with air to reduce the flow temperature to meet the thermal and structural requirements for turbine nozzle guide vanes. Indeed, for the typical combustor residence time in a conventional gas turbine, approximately half of the residence time is devoted to fuel vaporization and rapid mixing, and half of that is devoted dilution by mixing with air [1-4,16]. The fuel vaporization and rapid mixing can be modeled by the WSR model in a primary zone. Otherwise, the mixing of air for dilution can be modeled by the plug flow reactor (PFR) model in a secondary zone [1-4,16]. The main function of the dilution process in the secondary zone is to allow a sufficient convective residence time for the primary zone effluent to undergo full combustion. The combination of the WSR and PFR models to realize an ideal model for gas turbine combustors results in the well-known Bragg combustor [1-4,16].

In the present work, however, we used a premixed-fuel combustor with a configuration likely to be used in the reheating system of an aircraft engine modeled by a single WSR. A dilution process does not occur in the secondary zone and it is not necessary to apply the PFR model after the WSR model [14]. The basic three assumptions of the WSR model are as follows [1-4,16].

(a) A single limiting reaction governs the overall rate of combustion. We used the global reaction rate kinetics for the combustion model, as will be described later by Eq. (3.14). Although the combustion of hydrogen is an extremely complex process (33 reaction steps were proposed for the scramjet combustor kinetics by Jachimowski [17]), it may be analyzed on the assumption that combustion can be fully described by a single global reaction in which hydrogen and air react at a certain rate to form combustion products. This approach is based on the notion that a single limiting reaction governs the overall rate of combustion. Compared with the chemistry of the combustion process, this is an extremely rough assumption. Its justification lies entirely in the fact that a global reaction rate provides a major simplification while explaining experimental evidence to a satisfactory degree from the viewpoint of practical engineering. Indeed, the validity of assumption (a) has been demonstrated in previous works [5-8,16,18,19].

(b) The fuel and air premixture is fed into the combustor at a constant rate, and the burned material leaves the zone at a constant mass flow rate. Equation (3.14) given later implies that the reaction rate is a function of the static pressure and reaction temperature regardless of whether the flow regime is laminar or turbulent. The turbulence of the flow plays a minor role in increasing the reaction rate with increasing chemical parameter [14,16,20]. Thus, we can apply the WSR model to the laminar burning velocity, where the rapid reaction rates are governed by the static pressure and reaction temperature.

(c) The temperature and chemical composition of the burned material remain unchanged in the combustion zone.

A technical drawback of the WSR model is that the heat release rates are related to the reaction temperature [1,3] as will be shown later by Eq. (3.13). Equation (3.13) implies that the combustion efficiency depends on the reaction temperature. Thus, the combustion efficiency must be known a priori to estimate the reaction temperature [1,3]. However, this is a drawback in any calculation aiming to determine the combustion efficiency. For the burning velocity model described in Sec. 3.1, the combustion efficiency can be estimated from the combustor inlet static temperature, static pressure and geometry through experimentally obtained correlations without knowing the reaction temperature. The non-adiabatic operation or the effect of heat losses suggested by Spadaccini et al. [8] can be taken into account when determining the combustion efficiency corresponding to the θ parameter while taking heat losses into account as explained in greater detail in Sec. 3.1. A simplified atom-balance equation for the overall lean combustion reaction of the hydrogen-air premixture fuel is expressed as

$$\phi H_2 + \frac{1}{2}\left\{O_2 + \frac{79}{21}N_2\right\} \rightarrow \phi(1-\eta_c)H_2 + \phi\eta_c H_2O + \frac{1}{2}\left\{(1-\phi\eta_c)O_2 + \frac{79}{21}N_2\right\}, \tag{3.11}$$

The sum of the product molecular numbers is

$$N_{total} = \frac{50}{21} + \phi\left(1 - \frac{1}{2}\eta_c\right). \tag{3.12}$$

The static reaction temperature and combustion efficiency can be expressed as a linear equation by using the energy balance equation for the static enthalpy of the reactant and product gases [2-4],

$$T = T_6 + \eta_c(T_{AFT} - T_6) = T_6 + \eta_c\left(\frac{\phi f_{st} h_{H_2}}{C_p}\right), \tag{3.13}$$

where T_{AFT} is the adiabatic flame temperature and f_{st} is the stoichiometric mass-basis fuel-air ratio.

The third-order reaction of hydrogen with air is assumed as the global reaction rate mechanism. This assumption has been well supported by the research of the MIT group [5-8], in which the reaction time was estimated by considering the third-order reaction of hydrogen with air. In global reaction rate theory, the order of a reaction is the same as the exponent of the static pressure. Thus, the global reaction rate is proportional to the cube of the static pressure. Using Eqs. (3.11) to (3.13), the volumetric mass flow rate consumption of the hydrogen-air premixed fuel can be expressed by a modified Arrhenius equation for the overall combustion reaction,

$$RR_{H_2} = M_{H_2} Ar \exp\left(-\frac{E_a}{RT}\right)\left(\frac{P_6}{\overline{R}TN_{total}}\right)^3 \phi^2(1-\eta_c)^2(1-\phi\eta_c)\times 10^{-15}, \tag{3.14}$$

where RR_{H_2} is the volumetric mass rate of hydrogen consumption, M_{H_2} is the molecular weight of hydrogen, $Ar = 1.78\times 10^{17}\left(\left(cm^3/mole\right)^2/s\right)$ is the Arrhenius constant [18,19], $E_a = 7.2(kcal/mole)$ is the activation energy [18,19] and N_{total} is the total product molecular number. The conservation of fuel mass is applied to the steady-flow WSR control volume, which corresponds to the recirculation zone of the flameholder wake, to determine an alternative

form for the volumetric mass flow rate consumption:

$$RR_{H_2} = \left(\frac{\phi f_{st} \dot{m}_E}{V_{WSR}} \right) \eta_c \quad , \tag{3.15}$$

where $V_{WSR} = 11.4 \times 10^{-9} \left(m^3 \right)$ is the baffle wake region volume in the WSR model.

3.2.5 Combustion Stability

In practical gas turbine combustor, the WSR concept is applied to the entire volume of the chamber [1-4,16]. Equating the two equations for RR_{H_2} given by Eqs. (3.14) and (3.15) after substituting $\dot{m}_E \to \dot{m}_A$ and $V_{WSR} \to A_{ref} L_{ref} \equiv V_{chamber}$:

$$RR_{H_2} = M_{H_2} Ar \exp\left(-\frac{E_a}{RT} \right) \left(\frac{p_6}{\bar{R} T N_{total}} \right)^3 \phi^2 (1-\eta_c)^2 (1-\phi\eta_c) \times 10^{-15} = \left(\frac{\phi f_{st} \dot{m}_A}{V_{chamber}} \right) \eta_c \, . \tag{3.16}$$

Rearranging Eq. (3.16) by eliminating RR_{H_2} gives

$$I \equiv \frac{\dot{m}_A}{A_{ref} L_{ref} (P_6)^3} = \frac{M_{H_2} Ar \exp\left(-\frac{E_a}{RT} \right) \phi (1-\eta_c)^2 (1-\phi\eta_c) \times 10^{-15}}{\eta_c f_{st} \left(\bar{R} T N_{total} \right)^3} \, . \tag{3.17}$$

This is called the combustion loading parameter (CLP) [1-4,14]. The CLP reflects the effect of the airflow rate, combustor volume and static pressure on the combustion flame stability. By fixing the parameters on the right of Eq. (3.17), i.e., M_{H_2}, f_{st}, Ar, R, $\bar{R}$, E_a, η_c and ϕ (note that the reaction temperature T is related to η_c through Eq. (3.13) and N_{total} is related to ϕ and η_c through Eq. (3.12)), the theoretical value of $I = \frac{\dot{m}_A}{A_{ref} L_{ref} (P_6)^3}$ on the left of Eq. (3.17) can be solved [18,19]. By repeating the calculation for various values of ϕ while keeping the other seven parameters, i.e., M_{H_2}, f_{st}, Ar, R, $\bar{R}$, E_a and η_c, on the right of Eq. (3.17) constant, a complete stability map of the combustor can be obtained as shown in Fig.3.4.

In the limit of $I \to 0$, the residence time in the combustor volume is infinite and there is sufficient time for the chemical reaction to reach equilibrium. At the other limit of $I \to \infty$, the

residence time is zero and the reactants exit the combustor volume without undergoing a chemical reaction (blowoff). Therefore, the stability loop in Fig.3.4 indicates the boundary of the chemical reaction in which equilibrium can be reached. The experimental values of the CLP, i.e., $I_{exp} = \dfrac{\dot{m}_A}{A_{ref} L_{ref} (P_6)^3}$, must be located within the stability loop to demonstrate the validity of WSR theory. A demonstration of the validity of WSR theory will be described in Sec. 3.5.

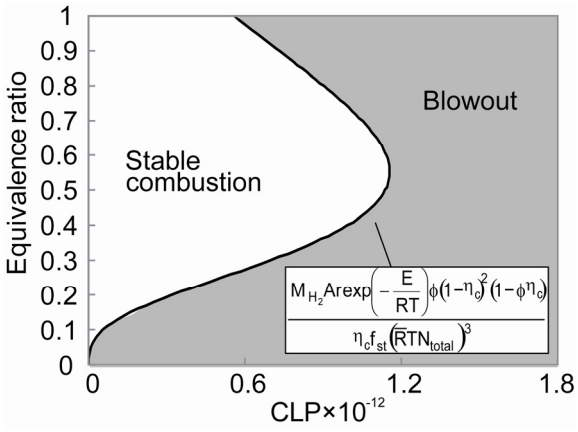

Fig.3.4 Combustion stability map on the basis of combustion loading parameter CLP

3.3 Microfabrication

Figure 3.5 shows a cross-sectional view of the prototype silicon microscale can combustor. The microscale can combustor is composed of seven microfabricated silicon wafers. An exploded view of the seven-wafer stack is shown in Fig.3.6. Wafer #1 includes the fuel and air intakes. The adjacent wafer #2 forms the premixing zone of the hydrogen fuel and air. Wafer #3 corresponds to the flameholder. The adjacent wafers #4 and #5 form the combustion chamber and cooling channel. Wafers #5, #6 and #7 form the combustion gas and cooling air discharge channels.

A 500 μm-thick silicon wafer is selected as the starting substrate. Both sides of the silicon wafer are patterned by ultraviolet (UV) lithography and etched by ICP-RIE. Each wafer is aligned and bonded together to form a multilayer silicon combustor assembly. Reference [21] describes similar wafer bonding in the fabrication of a multilayer microscale internal combustion engine.

The dimensions of the fuel ports in wafer #1 are critical, since the fuel ports have a 30 μm -diameter circular opening with a 250 μm hole length. The dimensions of the flameholder in wafer #3 are also critical in realizing the aero-thermodynamic design concept discussed in previous sections. Each flameholder has a 250 μm×250 μm square-shaped cross section and a 500 μm-deep trench. These microstructures are fabricated by ICP-RIE (etching conditions: 130

SCCM of SF_6 for 10 s cycle, 10 W platen power and 600 W coil power, followed by 80 SCCM of C_4F_8 for 5 s cycle, no platen power and 600 W coil power). Appropriate etching conditions for reducing the undercut (lateral) etching for the microhole, trench and wall structures and the dark regions composed of microscale masked silicon pillars were determined by preliminary experiments.

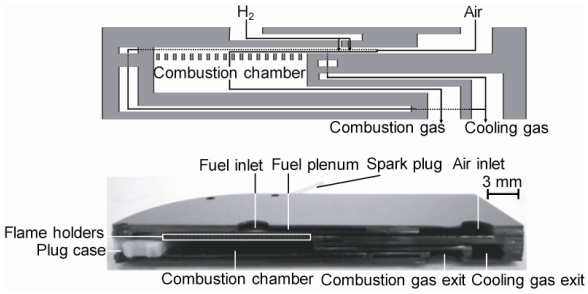

Fig.3.5 Cross-sectional views of prototyped silicon microscale can combustor

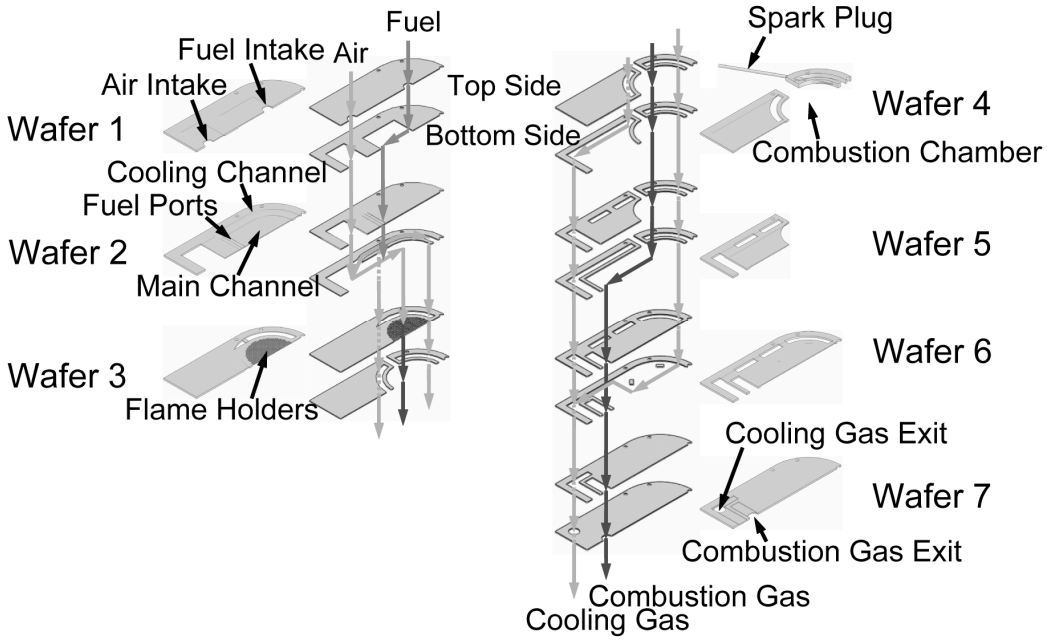

Fig.3.6 Exploded view of micro-fabricated seven silicon wafers (silicon microstructures were fabricated by MEMS process)

3.4 Experimental Procedure

Hydrogen is selected as a fuel owing to its relatively low ignition energy (~$2\text{x}10^{-5}$J at $\phi = 1$) and quenching distance (~0.64mm at $\phi = 1$). Hydrogen gas and air are separately supplied via an external gas feed system to the microscale can combustor. Figure 3.7 shows a photograph of the experimental setup. The microscale can combustor is mechanically mounted on a metal interface as shown in Fig.3.7. The metal interface connects the small-scale combustor to the large-scale external feed system, which includes a thermocouple used as a temperature sensor, a pressure sensor, and gas-inlet and discharge lines. The metal interface has several through ports with mechanical seals, and these ports are connected to the external gas feed system to supply fuel to the combustor and discharge combustion products from the combustor. The remaining ports are directly connected to 0.25 mm-diameter type-K thermocouples and piezoresistive pressure sensors, which can be used to measure the combustor exit, cooling gas and chamber wall temperatures and the total pressure loss. The unburned hydrogen concentration contained in the discharged combustion products can be measured using a commercial hydrogen concentration sensor. The ~1 mm small gap, corresponding to the height of a mechanical seal, between the surfaces of the metal interface and the microscale combustor outer walls contributes to the formation of a solid-gas-solid heat transfer boundary. Thus, the significant heat loss due to a direct solid-solid heat transfer boundary can be reduced.

The gauge pressures of the supplied gases are adjusted to 101.3 kPa by using pressure regulators. The fuel equivalence ratio is set using mass flow controllers. The spark igniter, whose energy exceeds $2\text{x}10^{-5}$J, is excited by a pulse signal from a function generator and is used to start microscale ignition. Mechanically machined 0.2 mm-diameter Pt microwire probes are used for the spark plugs owing to their resistance to erosion. Reference [21] contains more detail regarding the spark ignition system used for microscale combustion.

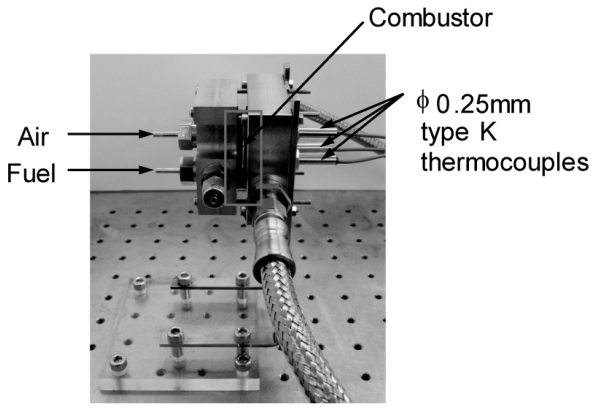

Fig.3.7 Photograph of experimental setup for microscale can combustor and related instruments

3.5 Experimental Results and Discussion

The microscale combustion tests were performed using a premixed hydrogen-air fuel. Fig.3.8 shows plots of the combustor exit temperature with the variation of the equivalence ratio. At equivalence ratios from 0.9 to 1.0, we observed unstable combustion phenomena: the lean combustion temperature decreased in spite of the increase in the equivalence ratio toward the stoichiometric condition ($\phi = 1.0$) or partial flame extinction occurred during operation. Thus, we classify these points as corresponding to blowoff. This is the primary reason why the temperature reaches a peak at the equivalence ratio of 0.8. Indeed, we also performed the experiments under rich conditions, although, we could not obtain reliable data owing to flame extinction.

Figure 3.9 shows plots of the corresponding overall combustor efficiency. The combustor produced a maximum exit gas temperature of 1350 K for a mass flow rate of 0.2g/s under ambient pressure. The maximum overall efficiency was 68% at the exit gas temperature of 1200 K. This may be an acceptable or borderline level for microscale turbomachinery applications. Previous works [5-8] show the same trend in the experimental results as that shown in Fig.3.9.

After the operation for several hours, no significant permanent deformation due to creep or fatal failure due to the discontinuous structure of the members (owing to the concentration of stress) was observed in the combustor.

3.5.1 Combustion Stability Based on Combustion Loading Parameter (CLP)

Figure 3.10 depicts a comparison of the combustion stability predicted by Eq. (3.17) and the experimental results. All the experimental data were located within the boundary of the stable combustion limit. The CLP is based on the WSR model with the chemical reaction parameters shown in Eq. (3.17). The accuracy of the CLP stated above depends on the definition of the global reaction rate equation given by Eq. (3.14). Therefore, it is not surprising that blowoff or flame extinction occurred in the region very close to the boundary of the stable combustion limit. In fact, the data for blowoff or flame extinction at an equivalence ratio in the vicinity of 1.0 were occurred very close to the boundary of the stable combustion loop (Fig.3.10). However, it is evident from the experiments that the use of a global reaction rate results in a major simplification while explaining the experimental results to a satisfactory degree from the viewpoint of practical engineering.

Fluid dynamic parameters such as the laminar flame structure are not taken into account in the CLP. Therefore, in the next section, we investigate the origin of the blowoff at an equivalence ratio of close to 1.0 from the viewpoint of the fluid dynamic parameters proposed by Zukoski [14].

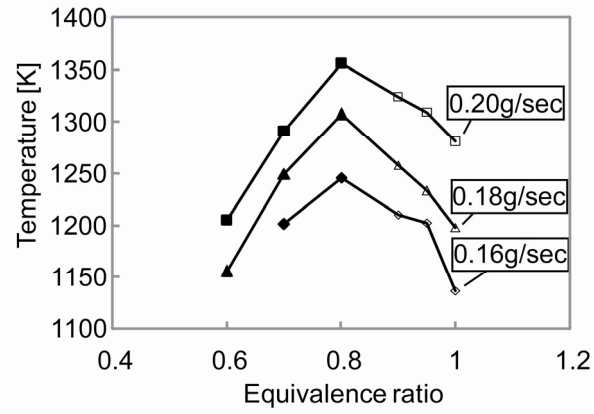

Fig.3.8 Experimental measurements for combustor exit temperatures with the variation of equivalence ratio

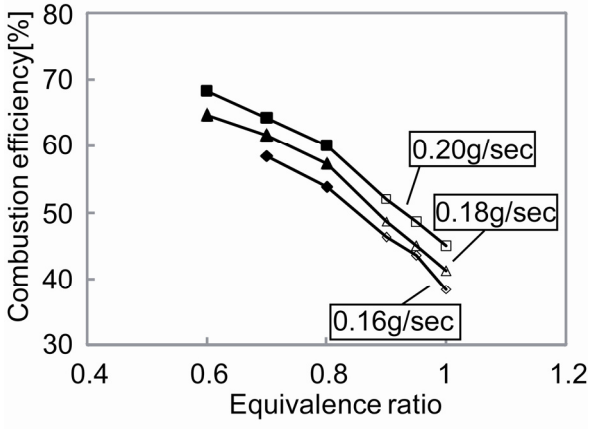

Fig.3.9 Experimental measurements for combustor efficiencies with the variation of equivalence ratio

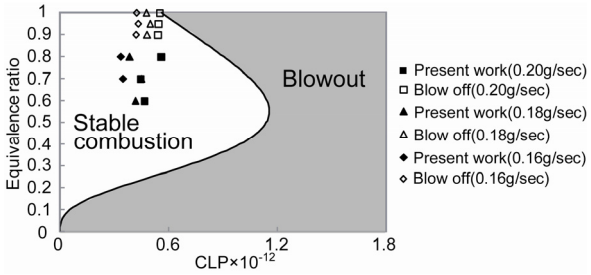

Fig.3.10 Comparison of prediction and experimental results for stable combustion operating space

3.5.2 Combustion Stability Based on Characteristic Chemical Time

The blowoff and flame extinction phenomena can be explained by examining the flame stability by consideration of the bluff bodies in the premixed flow. This approach is based on the wake of a two-dimensional flameholder as shown in Fig.3.11. As already mentioned in Sec. 3.2, the flameholder wake zone can be subdivided into the recirculation and mixing zones. The mixing zone separates the recirculation zone from the unburned premixed fuel in the wake of the flameholder. On the basis of a number of experiments on flameholders of various sizes, Zukoski [14] suggested that a characteristic chemical time, i.e., the period required to achieve ignition in the mixing zone in the flameholder wake flow, can be obtained from a set of flame blowoff experiments. In these experiments, the characteristic chemical time was related to the maximum length of the recirculation zone and the unburned gas velocity at the edge of the mixing zone as [14]

$$\tau_{chemical} = \frac{u_4}{L}. \tag{3.18}$$

From the viewpoint of practical engineering design, Lewis and von Elbe derived an expression equivalent to Eq. (3.18) by considering the burning velocity, the flame sheet thickness and the maximum possible unburned gas velocity at the edge of the mixing zone [14,22-24]. These parameters are easy to determine from experiments and simple calculations. Therefore, the blowoff condition can be expressed as

$$\tau_{chemical} \geq \frac{y}{S_u} = \frac{\log_{10}\left(\frac{u_{4\,max}}{S_u}\right)^{\frac{\delta_L}{0.434}}}{S_u}, \tag{3.19}$$

where y is the flame movement distance.

Zukoski [14] experimentally determined the characteristic chemical time τ_{exp} of hydrogen as a function of the equivalence ratio. The value of τ_{exp} is approximately independent of the flameholder geometry in gas turbine engine applications. Unfortunately, an independent theoretical calculation of τ_{exp} by considering the chemical kinetics of the reaction flow has yet a subject to be reported [25]. Therefore, in this paper we adopt the experimental value of τ_{exp} shown in Fig.3.12 in the subsequent discussion.

Figure 3.12 shows a comparison of the characteristic chemical times obtained experimentally by Zukoski [14] and by calculation using Eq. (3.19) plotted against the equivalence ratio. The

criterion for flame extinction, i.e., $\tau_{exp} \geq \frac{\log_{10}\left(\frac{u_{4\,max}}{S_u}\right)^{\frac{\delta_L}{0.434}}}{S_u}$, is satisfied for equivalence ratios from 0.8 to 1.0. The results of the experiment show that blowoff or flame extinction occurred at equivalence ratio from 0.8 to 1.0. Therefore, it is concluded that the combination of the CLP and the criterion in Eq. (3.19) is valid for the precise prediction of flame extinction along the boundary region of the stable combustion limit.

Shanbhogue et al. [24] stated in their review paper that there is general agreement that the blowoff process is controlled by the competition between fluid mechanical and chemical kinetic processes as implied by Eqs. (3.18) and (3.19). Shanbhogue et al. [24] lead to the same form of the correlation in terms of the Damköhler number, i.e.,

$$Da = \frac{\tau_{flow\ residence}}{\tau_{chemical\ reaction}}. \tag{3.20}$$

Since the pioneering work of Zukoski [14], a huge amount of data for the Damköhler number at blowoff as a function of the hydraulic diameter Re_D has been accumulated. The scaling equation proposed by Shanbhogue et al. [24] on the basis of the data is

$$Da \cong const.(Re_D)^{-0.67} \quad \left(const. \approx 5.0 \times 10^2\right). \tag{3.21}$$

A simple calculation based on Eq. (3.21) leads to $Re_D \cong 1.1x10^4$ at blowoff for our microscale combustor, and the corresponding Damköhler number was found to be $Da \cong 0.9$. Therefore, Eq. (3.21) provides alternative experimental evidence for the blowoff.

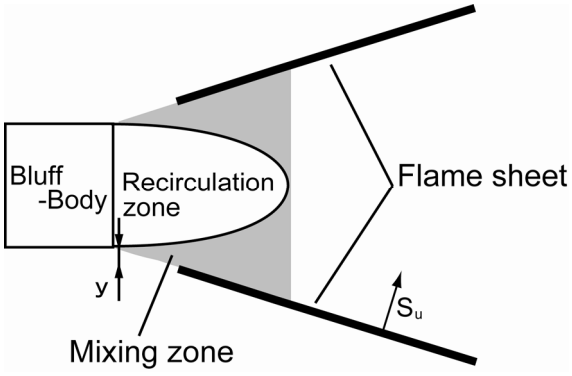

Fig.3.11 Schematic of flame holder wake two dimensional flame structure (highly simplified)

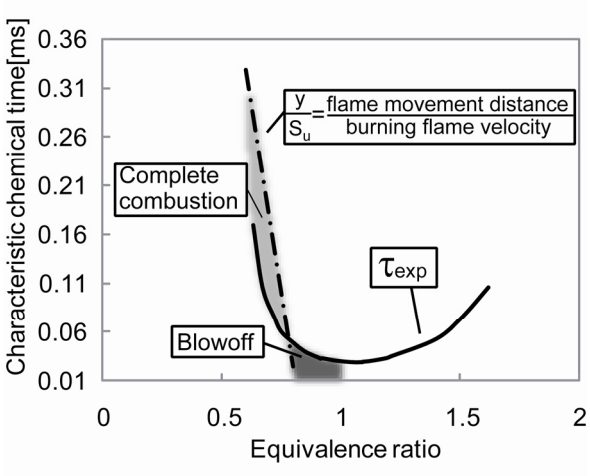

Fig.3.12 Comparison of calculation and experimental values for characteristic chemical time used for flame extinction criteria

3.5.3 Stagnation Pressure Drop of Combustor

The measured maximum stagnation pressure drop was less than 4% for the maximum mass flow rate of 0.2g/s. This may be an acceptable level for microscale turbomachinery applications. The stagnation pressure drop is proportional to the flow dynamic pressure based on the flow area of the combustor [20], i.e.,

$$\frac{\Delta P_0}{P_0} \propto \left(\frac{\gamma}{2}\right) M_b{}^2 . \tag{3.22}$$

Equation (3.22) implies that the stagnation pressure drop is a quadratic function of the Mach number of the burner area M_b. Indeed, a quadratic relation between the stagnation pressure drop and the mass flow rate was observed in our experiment.

3.5.4 Note on Cooling Effectiveness

The combustion chamber wall is heated by convection and radiation from the hot gas inside it. The relative contributions of convection and radiation to the total magnitude of heat transfer are important factors in maintaining wall temperature and stress below values causing material creep rupture and in calculating the magnitude of heat loss. Sufficient cooling air must be allocated to protect the combustion chamber from high convective and radiation heat loads due to combustion. As described in Sec. 3.3, the coolant air is introduced through the cooling channel in such a way that a film of air is formed between the inner wall of the combustor casing and the outer wall of the combustion chamber. The cooling effectiveness of the combustor can be generally defined as [2-4]

$$\Phi \approx \frac{T_g - T_w}{T_g - T_c}, \tag{3.23}$$

where T_g is the combustion gas temperature, T_w is the temperature of the solid silicon wall and T_c is the cooling air temperature. Typical experimental values of the cooling effectiveness for various cooling air mass flow rates are depicted in Fig.3.13 for a state-of-the-art aircraft gas turbine combustor [2-4]. $Fc \approx \frac{\dot{m}_{coolant}}{\dot{m}_A}$ is rate of the coolant flow in the cooling channel as a function of the main flow in the chamber. The experimental values for the cooling effectiveness of the microscale can combustor are also plotted in Fig.3.13. The experimental error originates from the thermal conductivity, radiation, the large temperature gradient along the type-K thermocouple and the calibration drift of the type-K thermocouple itself. The predicted uncertainty for the type-K thermocouple measurement is up to approximately $\pm 150K$.

A typical value of $\Phi \approx 0.7$ is feasible for $Fc \approx 0.5$. The average experimental wall temperature corresponding to the value of $\Phi \approx 0.7$ was estimated to be as high as 770 K, which is below the silicon creep temperature of 900 K [5,26]. In fact, after operation for several hours, the creep strain was estimated by direct dimensional measurement of the combustor using a scanning electron microscope. No significant permanent deformation due to creep (more than 0.01% creep strain) was observed in the combustor.

The above data suggest that a large flow fraction, i.e., a greater coolant flow, is required for the microscale combustor to achieve the same cooling effectiveness as its large-scale counterparts. However, a large coolant flow fraction causes an unfavorable and uncontrollable turbine inlet temperature profile, which is important for the high-temperature endurance of the nozzle guide vanes behind the combustor exit. The obtained experimental behavior is consistent with that for small aircraft gas turbine combustors reported by Garrett [27].

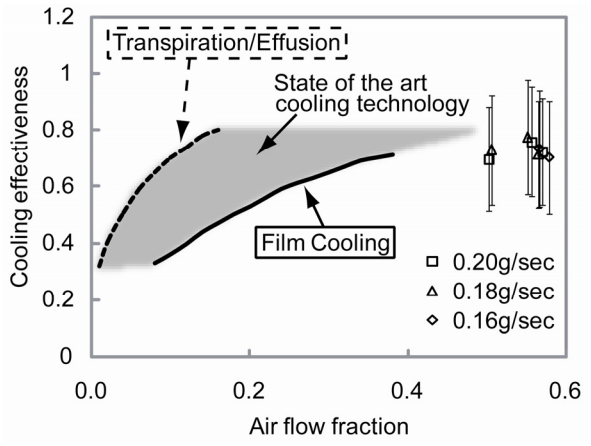

Fig.3.13 Experimental values of cooling effectiveness with the variation of flow fraction of coolant flow (state-of-the-art cooling technology for aircraft engine combustors were indicated as comparison)

3.5.5 Impact of Heat Transfer on Combustion Efficiency

In the absence of exact experimental or theoretical data for microscale combustors, an assumption has been made that classical straight-pipe heat transfer will hold inside the chamber. Waitz et al. recommended the use of the turbulent flow case, since this is more sensitive to the Reynolds number than the laminar flow case, i.e., $Nu_{D_h} \propto \sqrt[5]{(Re_{D_h})^4}$ [1,8,28]. This leads to an expression of the form [1]

$$E' \propto \frac{h_g}{D_h^{0.2}} \left(\frac{m_g}{A_L \mu_g} \right)^{0.8} A_L \left(T_g - T_w \right), \tag{3.24}$$

where E' is the heat lost and D_h is the hydraulic diameter of the chamber.

In the absence of exact data for microscale combustors, classical radiation from nonluminous and luminous gases is assumed to hold for heat transfer [1],

$$E' \propto \sigma \varepsilon_g T_g^{1.5} \left(T_g^{2.5} - T_w^{2.5} \right) A_L, \tag{3.25}$$

where ε_g is the gas emissivity at temperature T_g. The value of ε_g for nonluminous and luminous flames may be obtained from the following expression:

$$\varepsilon_g \propto p(\phi D_L)^{0.5} T_g^{-1.5}. \tag{3.26}$$

The uncooled chamber wall temperature can be determined from the heat transfer by convection and radiation. For a large-scale gas turbine chamber, the convection and radiation heat transfer processes have the same or a comparable order of magnitude regardless of the geometry and operation conditions of the system (order of $10^5\ W/m^2$ [1]). Scaling laws for heat loss due to convection and radiation can be determined from Eqs. (3.24) to (3.26). The obtained laws are $\frac{E'}{\dot{E}} \propto \frac{1}{D_h^{(6/5)}}$ and $\frac{E'}{\dot{E}} \propto \frac{1}{D_h^{(1/2)}}$, respectively. And $\dot{E}$ is the heat generated. The ratio of heat lost to heat generated can be scaled to an inverse power of the hydraulic diameter. For a microscale combustor, the typical ratio of heat lost due to convection to heat generated is two orders of magnitude greater than that of a large-scale combustor, while the heat lost due to radiation has the same order of magnitude. Therefore, for a microscale combustor, heat transfer by convection is dominant, and the contribution from radiation may be neglected. The scaling law of $\frac{E'}{\dot{E}} \propto \frac{1}{D_h^{(6/5)}}$ is consistent with that of Waitz et al. [7], who did not take the contribution from radiation into account.

The low effectiveness of cooling with a large flow fraction and the low combustion efficiency reflect the mechanism leading to large thermal loss mentioned above. For large-scale combustors, heat loss can be neglected, i.e., $\frac{E'}{\dot{E}} \sim 0.001 \text{ to } 0.01$ [1,2,11,12,28]. For microscale combustors, heat loss and heat generated are the same or have comparable orders, say, $\frac{E'}{\dot{E}} > \sim 0.1$. Therefore, more than 99% combustion efficiency is not feasible, and the heat transfer loss is a direct consequence of the relatively low combustion efficiency obtained from experiments.

3.5.6 Combustion Inefficiency due to Unused Chemical Energy

The combustion inefficiency due to unused chemical energy can be determined by measuring the hydrogen concentration in the combustion products [16]. The inefficiency can then be calculated using

$$\eta_i = \frac{(X)_{H_2}(h)_{H_2}}{\dot{m}_f h_f}, \tag{3.27}$$

where $(X)_{H_2}$ is the mass fraction of hydrogen determined by measurement and $(h)_{H_2}$ is the heat of combustion of hydrogen. Figure 3.14 shows η_i plotted against the equivalence ratio. Values of η_i of less than 10% were obtained regardless of the equivalence ratio. The contribution of the combustion inefficiency due to unused chemical energy is relatively small. Therefore, it can be concluded that the combustion efficiency is dominated by heat transfer for the microscale combustor. The experimental evidence shown in Fig.3.14 suggests that the assumption made for the single WSR model in Sec. 3.2.4 is appropriate for describing the overall performance of the premixed-fuel microscale combustor.

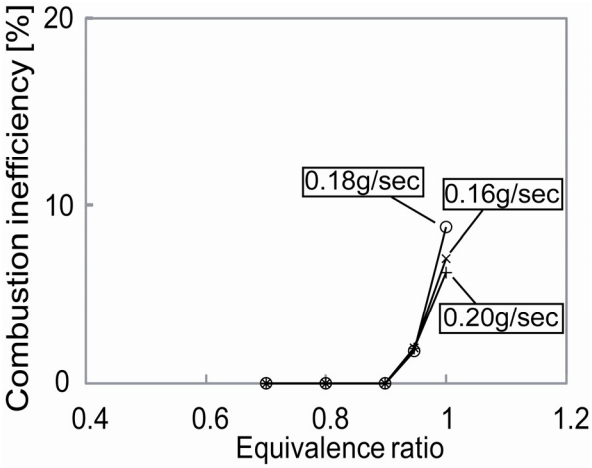

Fig.3.14 Combustion inefficiency due to unused chemical energy with the variation of equivalence ratio

3.6 Conclusion

The aero-thermodynamic performance of the microscale can combustor was designed with consideration of the burning velocity, WSR and CLP models. The relationship between the stable combustion operation space and the geometrical configuration and inlet thermodynamic quantities of the prototype microscale can combustor was experimentally investigated. The proposed aerothermodynamic model provides a rigorous physical interpretation of the performance of the microscale combustors investigated by the authors and those in previous works. It was concluded that the model can provide unified design guidelines for new microscale combustors having different dimensions, and configurations and unknown aero-thermodynamic performances.

References

[1] Lefebvre, A. H., and Ballal, D. R., 2010, Gas Turbine Combustion: Alternative Fuels and Emissions, 3rd ed., Taylor & Francis, New York, pp. 136–167.

[2] Henderson, R. E., and Blazowski, W. S., 1989, "Turbopropulsion Combustion Technology," Aircraft Propulsion Systems Technology and Design, G.C. Oates, ed., American Institute of Aeronautics and Astronautics, Inc., Reston, VA, pp. 105–165.

[3] Mattingly, J. D., Heiser, W. H., and Pratt, D. T., 2002, Aircraft Engine Design, 2nd ed., American Institute of Aeronautics and Astronautics, Inc., Reston, VA, Chap. 9.

[4] Mattingly, J. D., 2006, Elements of Propulsion: Gas Turbines and Rockets American Institute of Aeronautics and Astronautics, Inc., Reston, VA, p. 376; pp. 744–776.

[5] Epstein, A. H., 2004, "Millimeter-Scale, Micro-Electro-Mechanical Systems Gas turbine Engines," J. Eng. Gas Turbines Power, 125, pp. 205–226.

[6] Mehra, A., Zhang, X., Ayon, A. A., Waitz, I. A., Schmidt, M. A., and Spadaccini, C.M., 2000, "A Six-Wafer Combustion Systems for a Silicon Micro Gas Turbine Engine," J. Microelectromech. Syst., 9, pp. 517–527.

[7] Waitz, I. A., Gauba, G., and Tzeng, Y. S., 1998, "Combustors for Micro – Gas Turbine Engines," J. Fluid Eng., 120, pp. 109–117.

[8] Spadaccini, C. M., Mehra, A., Lee, J., Zhang, X., Lukachko, S., and Waitz, I. A., 2003, "High Power Density Silicon Combustion Systems for Micro Gas Turbine Engines," J. Eng. Gas Turbines Power, 125, pp. 709–719.

[9] Shan, X. C., Wang, Z. F., Jin, Y. F., Wu, M., Hua, J., Wong, C. K., and Maeda, R., 2005, "Studies on a Micro Combustor for Gas Turbine Engines," J. Micromech. Microeng., 15, pp.S215–S221.

[10] Hua, J., Wu, M., and Kumar, K., 2005, "Numerical Simulation of the Combustion of Hydrogen-Air Mixture in Microscaled Chambers Part II: CFD Analysis for a Micro-Combustor," Chem. Eng. Sci., 60, pp. 3507–3515.

[11] Lefebvre, A. H., 1966, "Theoretical Aspects of Gas Turbine Combustion Performance," CoA Note Aero, No. 163, Cranfield University, UK, pp.1–17.

[12] Greenhough, V. W., and Lefebvre, A. H., 1957, "Some Application of Combustion Theory to Gas Turbine Development," Sixth International Symposium on Combustion, Reinhold, New York, pp. 858–869.

[13] Wright, F. H., 1959, "Bluff Body Flame stabilization: Blockage Effects," Combust. Flame, 3, pp. 319–337.

[14] Zukoski, E. E., 1985, "Afterburners," Aerothermodynamics of Aircraft Engine Components, G. C. Oates, ed., American Institute of Aeronautics and Astronautics, Inc., Reston, VA, pp. 62–105.

[15] Greitzer, E. M., Tan, C. S., and Graf, M. B., 2006, Internal Flow, Cambridge University Press, Cambridge, UK, Chap. 1.

[16] Blazowski, W. S., 1985, "Fundamentals of Combustion," Aerothermodynamics of Aircraft Engine Components,, G. C. Oates, ed., American Institute of Aeronautics and Astronautics, Inc., Reston, VA, pp. 3–43.

[17] Jachimowski, C. J., 1988, "An Analytical Study of the Hydrogen-Air Reaction Mechanism with Application to Scramjet Combustion," NASA TP-2791.

[18] Coffee, T. P., Kotlar, A. J., and Miller, M. S., 1983, "The Overall Reaction Concept in Premixed, Laminar, Steady-State Flames. I. Stoichiometries," Combust. Flame, 54, pp. 155–169.

[19] Coffee, T. P., Kotlar, A. J., and Miller, M. S., 1984, "The Overall Reaction Concept in Premixed, Laminar, Steady-State Flames. II. Initial Temperatures and Pressures," Combust. Flame, 58, pp. 59–67.

[20] Kerrebrock, J. L., 1992, Aircraft Engine and Gas Turbines, 2nd ed., The MIT Press, Cambridge, MA, Chap. 4.

[21] Suzuki, Y., Okada, Y., Ogawa, J., and Toriyama, T., 2008, "Experimental Study on Mechanical Power Generation from MEMS Internal Combustion Engine, Sensors Actuators, A, 141, pp. 654–661.

[22] Lewis and von Elbe, G., 1987, Combustion, Flames and Explosions of Gases, 3rd ed., Academic Press Inc., New York, Chap. 2.

[23] Beer, J. M. and Chigier, N. A., 1972, Combustion Aerodynamics, Applied Science Publishers, Ltd., London, pp. 63–72.

[24] Shanbhogue, S. J., Husain, S., and Lieuwen, T., 2009, "Lean Blowoff of Bluff Body Stabilized Flames: Scaling and Dynamics," Prog. Energy Combust. Sci., 35, pp. 98–120.

[25] Radhakrishnan, K., and Pratt, D. T., 1988, "Fast Algorithm for Calculating Chemical Kinetics in Turbulent Reacting Flow," Combust. Technol. Sci., 58, pp. 155–176.

[26] Moon, H. S., Choi, D., and Spearing, S. M., 2004, "Development of Si-SiC Hybrid Structures for Elevated Temperature Micro-Turbomachinery," J. Microelectromech. Syst., 13, pp. 676–687.

[27] Leyes, R. A., and Fleming, W. A., 1999, The History of North American Small Gas Turbine Aircraft Engines, American Institute of Aeronautics and Astronautics, Inc., Reston, VA, pp. 11–26.

[28] B.Lakshminarayana, "Fluid Dynamics and Heat Transfer of Turbomachinery", John Willey & Sons, Inc., 1996.

Chapter 4

Summary and Conclusions

4.1 Aerodynamic Design Recommendations for Continuum Nozzle Flow

Figure 4.1 shows a comparison of the calculated operation envelope of the governing equation of motion and our experimental data. Figure 4.2 shows a comparison of the calculated relationship between Nu and $(2x/d_H)/(RePr)$, and our experimental data. Figure 4.3 also shows a comparison of the calculated relationship between Nu and Kn, and our experimental data. The value of Kn varies along the downstream of the channel throat. However, the value of Kn at the discharge section is approximately the same as that of the throat section for each device indicated in Figs.2.4 and 4.3. Each device has the favorable density (pressure) gradient along the divergent and straight channel sections. This leads to the density reduction (increment of the mean free path) and the increment of the geometric dimension (increment of the characteristic length) along the downstream of the divergent section of nozzle flow. As a consequence, the Kn maintains an approximately constant value along the downstream of the channel throat. Therefore, from a practical engineering viewpoint, the value of Kn at the throat section is adopted for each device. It is concluded from these figures that our experimental data can be plotted in the ranges of $Kn \cong 0.001$ and $Nu \cong 15$, where the application of the continuum Navier–Stokes equations and laminar heat transfer model is valid. The design recommendations for new microscale nozzles are summarized as follows.

(A) Governing equation of motion

As explained in Sec. 2.1.1, an operation envelope of the governing equation of motion for a new design device can be represented as a function of the nozzle characteristic length L and the working fluid parameters L/δ, δ/d, and Kn. A comparison of the operation envelope of the governing equation of motion and a new design specification obtained from the nozzle characteristic length and working fluid property can be carried out by using a map, as shown in Fig.2.2, confirming that the new design specification can be plotted within the continuum flow region. Note that if the plot is located outside of the continuum flow region, a governing equation of motion based on the statistical approach must be used and the following procedure is not valid.

(B) Effect of degree of nonadiabatic operation on microscale nozzle flow

The relationship between Nu, Kn, and a new design data obtained from the nozzle characteristic length and the working fluid property is plotted on the map, as shown in Figs. 2.3 and 2.4, in order to determine whether the heat transfer model is appropriate for the new design specification.

(C) Determination for preliminary nozzle geometry

The method of characteristics with weak waves is applied to the preliminary design of the divergent section of the microscale nozzle. The problem in this method is that the flow should be expanded from sonic at the throat to supersonic in the discharge section. We chose the appropriate Prandtl–Meyer function that corresponds to the design discharge Mach number.

(D) Calculation of nonadiabatic operation of microscale nozzle flow

Next, an original differential equation is derived to solve an aerodynamic problem that takes into account the cross-sectional area change, the adiabatic flow with friction, and the nonadiabatic flow with wall heat transfer,

$$dM^2 = F_A \frac{dA}{A} + \frac{M^2\left(1+\gamma M^2\right)}{1-\gamma M^2}\frac{dT}{T} + \frac{2TF_{cf}\,Pr^{2/3}}{T_w - T\left(1+R\dfrac{\gamma-1}{2}M^2\right)}\left(\frac{1-M^2}{1-\gamma M^2}\right)\frac{dT}{T} \quad \text{(Eq.(2.23))}.$$

The numerical integration of Eq. (2.23) for a design control volume leads to the variation in Mach number with respect to procedures (A)-(C). Finally, the calculation of the stagnation-to-static pressure ratio p_0/p against the throat-to-discharge cross-sectional area ratio A^*/A is carried out on the basis of Eq. (2.23), as shown in Fig. 2.16. This is the design aerodynamic performance map we aim to obtain. A repeat calculation involving procedures (A)-(D) until a satisfactory result is obtained may be necessary.

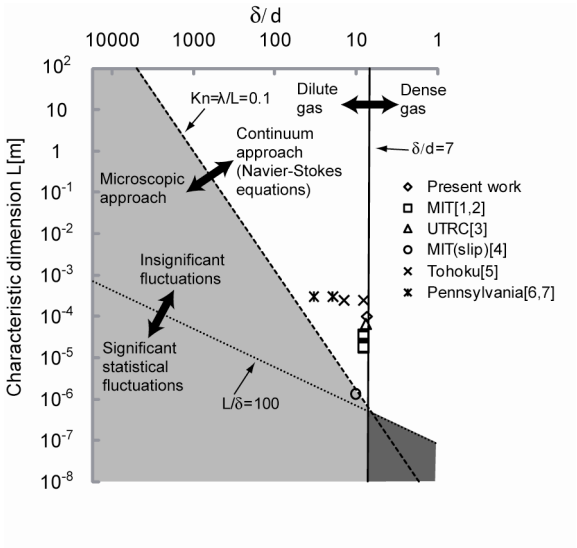

Fig.4.1 Comparison of calculated operation envelope of the governing equation of motion and present experimental data (MIT [1,2], UTRC [3], MIT (silp) [4], Tohoku [5], and Pennsylvania [6,7])

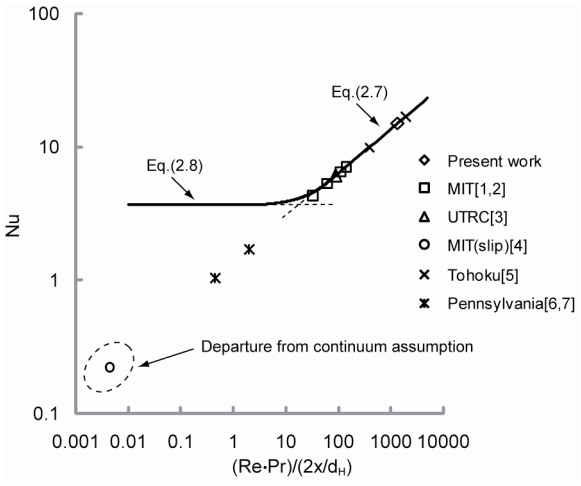

Fig.4.2 Comparison of experimental relationship between Nu and $\frac{2x/d_H}{RePr}$ (MIT [1,2], UTRC [3], MIT (silp) [4], Tohoku [5], and Pennsylvania [6,7])

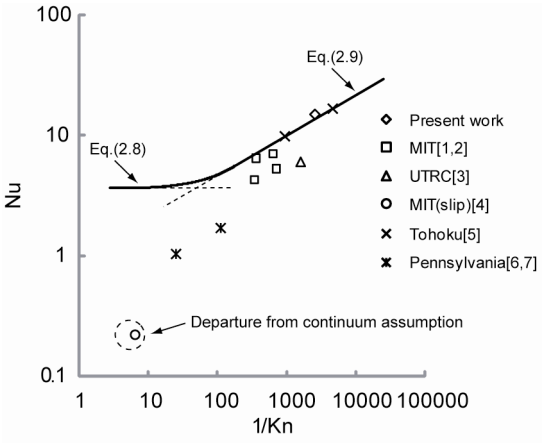

Fig.4.3 Comparison of experimental relationship between Nu and Kn (MIT [1,2], UTRC [3], MIT (silp) [4], Tohoku [5], and Pennsylvania [6,7])

4.2 Aero-thermodynamic Design Recommendations for Microscale Combustor

Figure 4.4 depicts a diagram that was first proposed by Lefebvre and Ballal [8] on the basis of the burning velocity model. The experimental data for microscale and conventional combustors are located within the region predicted by Lefebvre and Ballal [8]. Therefore, the combustion efficiency has a strong correlation with the value of θ defined in Eq. (3.3) regardless of the scale and geometrical configuration of the combustors. The experimental results of SIMTEC exhibit a large amount of scattering and do not appear to follow the theoretical model. The experimental combustion efficiencies were not reported in the SIMTEC paper [9], and the data plotted in Fig.4.5 were taken from the results of CFD simulations carried out by SIMTEC [10]. This may be the primary reason for the weak correlation of the data. In spite of the large amount of the scattering for the SIMTEC data, the data were located between the upper and lower bands of the performance curve based on the θ parameter as shown in Fig.4.4. Unfortunately, the amount of available data for empirically determining the correlation for the microscale combustor is extremely limited to date. Therefore, we decided to include the SIMTEC data for reference.

Figure 4.5 depicts the stable combustion limit as a function of the equivalence ratio and the CLP given by Eq. (3.17). The experimental values of the CLP i.e., $I_{exp} = \dfrac{\dot{m}_A}{A_{ref} L_{ref} (P_6)^3}$, with the variation of the equivalence ratio obtained from MIT, SIMTEC and the present work are located within the predicted stable combustion limits regardless of the geometrical configurations of the combustors. Therefore, it is concluded, from a practical engineering viewpoint, that aero-thermodynamic design based on the burning velocity, WSR and CLP models can provide unified design guidelines for microscale combustors having different

dimensions and configurations. The design recommendations for new microscale combustors are summarized as follows.

(A) Specification of combustion efficiency

Microscale heat transfer prevents the occurrence of a complete energy transformation (leading to non-adiabatic operation) as discussed in Sec. 3.1. Therefore, for a first prototype design, a combustion efficiency of more than 90% is not feasible, and the selection of the θ parameter with a value above the knee point in Fig. 3.1(a) ($\theta \cong 5$) may not be feasible without the selection of sophisticated materials or advanced thermal management. For critical microscale combustor design, selection of the right boundary value of the performance curve (the upper band for θ) is recommended to account for the strong heat loss effect due to the large surface area to volume ratio.

(B) Calculation of dimensions of combustion chamber

By fixing the values of P_6, T_6 and $\dot{m}_A$ corresponding to the combustor inlet conditions, an appropriate value of $A_{ref}(L_{ref})^{0.75}$ can be obtained from Fig.3.1(a) by reading off the value of θ at the point along the horizontal axis within the enclosed area at the required combustion efficiency. The chamber volume can be determined from the value of $A_{ref}(L_{ref})^{0.75}$ and Eq. (3.10) for the flame height.

(C) Prediction of stable operation space of combustor

The CLP is depicted as a function of the equivalence ratio in Fig.3.4, which can be used to specify the stable operation space of the combustor. The stability combustion loop of the CLP can be determined from the right of Eq. (3.17) as $\dfrac{M_{H_2} Ar \exp\left(-\dfrac{E_a}{RT}\right)\phi(1-\eta_c)^2(1-\phi\eta_c)\times 10^{-15}}{\eta_c f_{st}\left(\bar{R}TN_{total}\right)^3}$. The left of Eq. (3.17), $\dfrac{\dot{m}_A}{A_{ref}L_{ref}(P_6)^3}$, can be determined from procedures (A) and (B). This value should be located within the stability combustion loop for stable combustion obtained from the right of Eq. (3.17). A repeat calculation involving procedures (A) to (C) until a satisfactory result is obtained may be necessary.

Smaller combustion loading, corresponding to a smaller value of the CLP, may lead to a conservative stable combustion limit. However, this leads to a larger chamber volume and consequently a larger combustor. In contrast, a design with high combustion loading has a

stable combustion limit in the vicinity of the boundary described by the CLP. In the stable combustion limit, checking of the criterion for flame extinction is recommended to ensure a safe design.

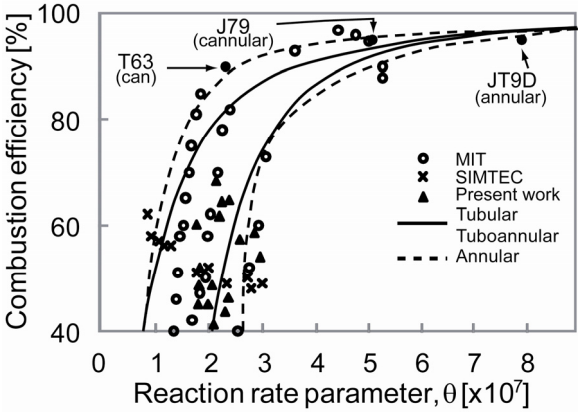

Fig.4.4 Correlation between combustion efficiencies for silicon microscale combustors and Lefebvre's θ parameters ($\theta \equiv \frac{(P_6)^{1.75} A_{ref} (L_{ref})^{0.75} \exp(T_6/300)}{\dot{m}_A}$)[8]

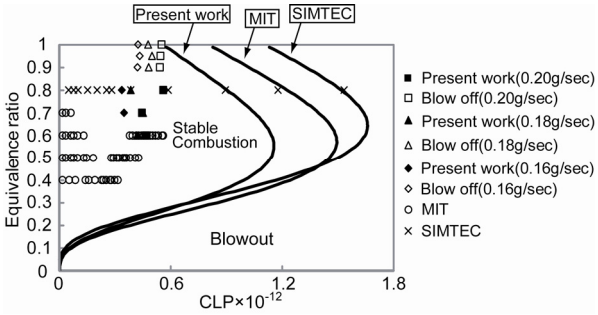

Fig.4.5 Comparison of predictions and experimental results for stable combustion operating spaces obtained from past and present works (previous works were reported by MIT [11-14] and SIMTEC [9])

References

[1] Bayt, R. L., and Breuer, K. S., 1998 "Viscous Effects in Supersonic MEMSFabricated Nozzles," Proceedings of the 1998 ASME International Mechanical Engineering Congress and Exposition, Anaheim, CA, ASME. New York, pp. 117–123.

[2] Bayt, R. L., 1999, "Analysis, Fabrication and Testing of a MEMS-Based MicropropulsionSystem," Ph.D. thesis, Department of Aeronautics and Astronautics, MIT, Cambridge, MA.

[3] Bayt, R. L., and Kenneth, S. B., 2001, "Analysis and Testing of a Silicon Intrinsic-Point Heater in a Micropropulsion Application," Sens. Actuators, A, 91, pp. 249–255.

[4] Arkilic, E. B., Schmidt, M. A., and Breuer, K. S., 1997, "Gaseous Slip Flow in Long Microchannels," J. Microelectromech. Syst., 6, pp. 167–178.

[5] Nagai, H., Naraoka, R., Sawada, K., and Asai, K., 2008, "Pressure-Sensitive Paint Measurement of Pressure Distribution in a Supersonic Micronozzle," AIAA J., 46, pp. 215–222.

[6] Alexeenko, A. A., Fedosov, D. A., Gimelshein, S. F., Levin, D. A., and Collins, R. J., 2006, "Transient Heat Transfer and Gas Flow in a MEMS-Based Thruster," J. Microelectromech. Syst., 15, pp. 181–194.

[7] Alexeenko, A. A., Levin, D. A., Fedosov, D. A., Gimelshein, S. F., and Collins, R. J., 2005, "Performance Analysis of Microthrusters Based on Coupled Thermal-Fluid Modeling and Simulation," J. Propul. Power, 21, pp. 95–101.

[8] Lefebvre, A. H., and Ballal, D. R., 2010, Gas Turbine Combustion: Alternative Fuels and Emissions, 3rd ed., Taylor & Francis, New York, pp. 136–167.

[9] Shan, X. C., Wang, Z. F., Jin, Y. F., Wu, M., Hua, J., Wong, C. K., and Maeda, R., 2005, "Studies on a Micro Combustor for Gas Turbine Engines," J. Micromech. Microeng., 15, pp.S215–S221.

[10] Hua, J., Wu, M., and Kumar, K., 2005, "Numerical Simulation of the Combustion of Hydrogen-Air Mixture in Microscaled Chambers Part II: CFD Analysis for a Micro-Combustor," Chem. Eng. Sci., 60, pp. 3507–3515.

[11] Epstein, A. H., 2004, "Millimeter-Scale, Micro-Electro-Mechanical Systems Gas turbine Engines," J. Eng. Gas Turbines Power, 125, pp. 205–226.

[12] Mehra, A., Zhang, X., Ayon, A. A., Waitz, I. A., Schmidt, M. A., and Spadaccini, C.M., 2000, "A Six-Wafer Combustion Systems for a Silicon Micro Gas Turbine Engine," J. Microelectromech. Syst., 9, pp. 517–527.

[13] Waitz, I. A., Gauba, G., and Tzeng, Y. S., 1998, "Combustors for Micro – Gas Turbine Engines," J. Fluid Eng., 120, pp. 109–117.

[14] Spadaccini, C. M., Mehra, A., Lee, J., Zhang, X., Lukachko, S., and Waitz, I. A., 2003, "High Power Density Silicon Combustion Systems for Micro Gas Turbine Engines," J. Eng. Gas Turbines Power, 125, pp. 709–719.

Appendix A

Introduction to Burning Velocity Model

A.1 Theory of Burning Velocity Model

The burning velocity model was first proposed by Greenhough and Lefebvre [1] in order to derive the dominant parameters that correlate with experimental data on combustion efficiency obtained from a wide range of pressures, temperatures, and air mass flow rates of combustion chambers having different configurations and dimensions. The concept of the model was established in the 1950s and made extremely rough assumptions. However, its justification still lies entirely in the fact that the parameters provide a major simplification while correlating with experimental data to a satisfactory degree from the viewpoint of practical new engine design. The model is reviewed briefly in this Appendix. For further details, please refer to the original paper and to the excellent text book of Lefebvre, Halls and Ballal. [2,3].

The combustion zone is regarded as being similar in structure to the flame produced by a Bunsen burner under turbulent flow conditions. The combustion performance can be described as a function of the ratio of the turbulent burning velocity to the velocity of the fresh mixture entering the combustion zone. It is assumed that all the fuel burns under complete combustion. Combustion inefficiency arises from the condition that some of the mixture passes through the combustion zone without undergoing combustion.

Combustion efficiency is defined as

$$\eta_c = \frac{\text{heat released in combustion}}{\text{heat available in fuel}} = \frac{\rho A_f S_T C_p \Delta T}{q\dot{m}_A H}, \tag{A.1}$$

where $C_p \Delta T = qH$ by definition. The flame area A_f is assumed to be proportional to the combustor reference area A_{ref}. Thus, Eq. (A.1) simplifies to

$$\eta_c \propto \frac{S_T}{U_{ref}}, \tag{A.2}$$

where $U_{ref} \propto \frac{\dot{m}_A}{A_{ref}}$.

According to the historical paper by Damköhler [4], the turbulent burning velocity may be related to the laminar burning velocity by the following equation:

$$S_T \propto S_L \, Re^a = S_L \left(\frac{U_j L_{ft} \rho}{\mu} \right)^a . \qquad (A.3)$$

The above expression for the Reynolds number is the same as that used in [1] and [2], except that the chamber reference velocity has been replaced by the primary zone air injection velocity. This is an improvement on the original theory since, in practice, the level of turbulence is affected by the air injection velocity and not the chamber reference velocity.

It can readily be shown that

$$U_j = U_{ref} \left(\frac{\Delta P_{ft}}{C_{ref}} \right)^{0.5} , \qquad (A.4)$$

where $\frac{\Delta P_{ft}}{C_{ref}}$ is the flame-tube pressure loss factor. Substituting Eq. (A.4) into Eq. (A.3) gives

$$S_T = S_L \left(\frac{U_{ref} L_{ft} \rho}{\mu} \right)^a \left(\frac{\Delta P_{ft}}{C_{ref}} \right)^{0.5a} . \qquad (A.5)$$

The laminar burning velocity S_L varies with both pressure and temperature. The variation of S_L with pressure may be expressed as a function of the power of the order of the reaction n, i.e., $S_T \propto S_L \propto P^{(n-2)/2}$. The variation of S_L with temperature is more complicated than that with pressure since it depends on the type of fuel and the fuel/air ratio. Semenov proposed a theoretical equation but it is too complex for practical application [5]. In the absence of appropriate experimental data to date, the variation of S_L with temperature may be predicted from reaction rate theory as will be shown later see Eq. (A.8). Therefore, it is appropriate to remove the temperature terms for a bimolecular reaction. The substitution of Eq. (A.5) into Eq. (A.3) and then Eq. (A.3) into Eq. (A.2) yields

$$\eta_c = f\left[\frac{(PL_{ft})^{\frac{a}{1-a}}\left(\frac{\Delta P_{ft}}{C_{ref}}\right)^{\frac{0.5a}{1-a}}}{U_{ref}}\right], \tag{A.6}$$

where $U_{ref} \propto \frac{\dot{m}_A}{P_6 A_{ref}}$, $L_{ft} \propto L_{ref}$, and $m = \frac{a}{1-a}$. The substitution of these expressions into Eq. (A.6) gives

$$\eta_c = f\left[\frac{P_6 A_{ref}(P_6 L_{ref})^m\left(\frac{\Delta P_{ft}}{C_{ref}}\right)^{0.5m}}{\dot{m}_A}\right]. \tag{A.7}$$

Finally the correlating parameter, which includes a temperature term derived from reaction rate theory [1], is of the form

$$\eta_c = f\left[\frac{P_6 A_{ref}(P_6 L_{ref})^m \exp(T_6/b)}{\dot{m}_A}\left(\frac{\Delta P_{ft}}{C_{ref}}\right)^{0.5m}\right]. \tag{A.8}$$

Lefebvre and Halls [2] demonstrated that combustion efficiency data obtained from low-pressure tests on combustion chambers having different configurations and dimensions could be satisfactorily correlated with Eq. (A.8) by substituting the values of $m = 0.75$ and $b = 300$. Neglect of the pressure loss term, which can be expected to be almost independent of the combustion chamber configuration and dimensions, leads to the well-known θ parameter

$$\eta_c = f(\theta) = f\left[\frac{(P_6)^{1.75} A_{ref}(L_{ref})^{0.75} \exp(T_6/300)}{\dot{m}_A}\right]. \tag{A.9}$$

Equation (A.9) has been applied with considerable success to the correlation of experimental data on combustion efficiency, and has proved very useful in reducing the amount of rig testing required to evaluate new combustor designs [3,6].

A.2 Application of Burning Velocity Model

Equation (A.9) provides a relationship between the combustion efficiency and the dimensions and operating conditions of a combustion chamber. For any given combustion chamber, the dimensions are constant and Eq. (A.9) may be rewritten as

$$\eta_c = f(\theta) = f\left[\frac{(P_6)^{1.75}\exp(T_6/300)}{\dot{m}_A}\right]. \qquad (A.10)$$

As shown in Fig.A.1, only a few test points are needed to establish the complete performance curve for a chamber. Furthermore, it is possible to predict combustion efficiencies with reasonable accuracy under flow conditions that lie outside the capacity of the rig testing facility. The correlation of Eq. (A.10) may be weak for conditions where the effects of atomization and heat losses become significant. Fortunately, such conditions lie outside the range of normal large-scale gas turbine engines [3,6].

A new combustor design may be largely based on past experience. A useful means of accumulating past experience is through the use of diagrams. For example, combustion efficiency data from all known combustors can be plotted against all the relevant variables. Such a diagram is shown in Fig.A.2, in which combustion efficiency is plotted against θ. In this figure, the enclosed areas depict experimental data obtained from a large number of current designs of tubular (can), tubo-annular (can-annular), and annular chambers. Figure A.2 can be used to determine the dimensions of a chamber required to satisfy the performance specifications in the preliminary design stage. The most severe operating conditions of a combustor are at the minimum inlet pressure P_6. Fortunately, this invariably corresponds to a high-altitude off-design condition at which a low combustion efficiency, say 80%, may be tolerated. Appropriate values of A_{ref} and L_{ref} can be obtained from Fig.A.2 by reading off the value of θ at the point along the horizontal axis within the enclosed area at the required combustion efficiency. Then, the values of A_{ref} and L_{ref} can be obtained by substituting the values of P_6, T_6, and $\dot{m}_A$ corresponding to 80% combustion efficiency. The actual point chosen represents a balance between the conflicting needs of high performance and low development cost [3,6].

In practice, it is difficult to estimate the primary zone mixture strength at the design stage. However, one can obtain a sufficient amount of data about the actual primary zone mixture strength and related important performances of the combustion process by inspection of the θ curves. This can be understood from Fig.A.3, which shows that any given θ curve actually

represents the combined performance of the primary and secondary zones (and also the dilute zone at very low pressures). The broken line drawn from the origin represents the primary zone combustion efficiency plotted against θ. An increase in burning velocity leads to a steeper slope of this line. The value of combustion efficiency is reached at the upper limit when all the fuel has been consumed. At the upper limit, the combustion efficiency is less than 100% owing to losses due to the chemical dissociation of the combustion products. The main function of the dilution process in the secondary zone is to allow sufficient convective residence time for the primary zone effluent to undergo full combustion. The secondary zone performance is represented by the broken line drawn from the origin corresponding to the maximum (upper limit) combustion efficiency attained in the primary zone. The unbroken line in Fig.A.3 describes the combined performance of the primary and secondary zones and indicates the level of combustion efficiency actually measured in practice [1,6]. In the present work, however, we used a premixed-fuel combustor with a configuration likely to be used in the reheating system of an aircraft engine. A dilution process does not occur in the secondary zone.

When the pressure is reduced, it should be possible in theory to maintain a high combustion efficiency by reducing the mass flow. However, with falling gas pressure, the atomization quality deteriorates and heat losses become more significant, and thus there is a minimum pressure below which combustion is impossible, i.e., blowout occurs. The effects of poor atomization and large heat losses are indicated in Fig.A.3 by the manner in which the lower portion of the overall performance curve falls away from the broken line to intercept the horizontal line at a finite value of θ [1,6]. Therefore, the burning velocity model, which accounts for the heat loss effect, can be represented by the minimum chamber dimensions required to maintain combustion. As shown in Sec.3.5.5, heat losses become significant for microscale combustors; however, the experimental evidence shows that the correlation given by Eq. (A.10) is still valid for microscale combustors.

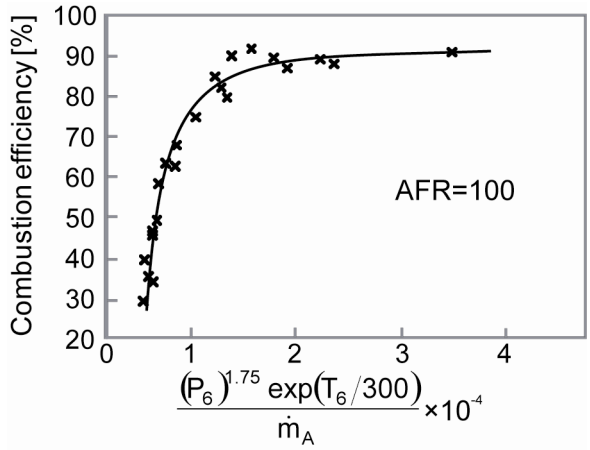

Fig.A.1 Correlation of combustion-efficiency data for an aircraft combustor [3]

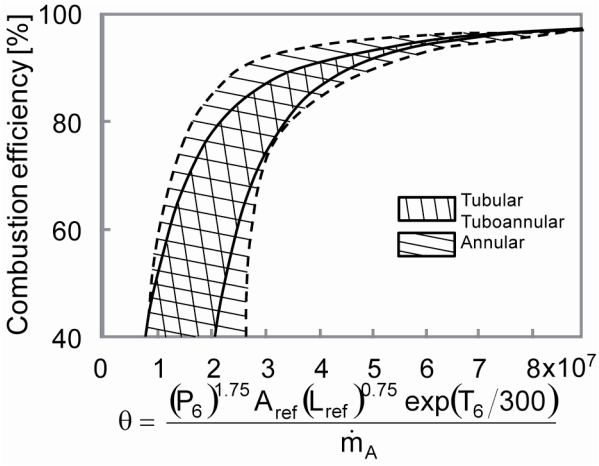

Fig.A.2 Design chart for conventional combustors [3,6]

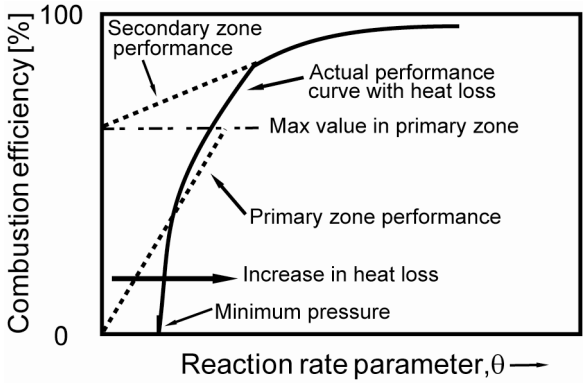

Fig.A.3 Theoretical curve of combustion efficiency[1,6]

References

[1] Greenhough, V.W., and Lefebvre, A. H., 1957, "Some Applications of Combustion Theory to Gas Turbine Development," Sixth Symposium (International) on Combustion, Reinhold, New York, pp.858–869.

[2] Lefebvre, A. H., and Halls, G.A., 1959, "Some Experiences in Combustion Scalling," AGARDO-graph 37, Pergamon Press Ltd, New York, pp.177–204.

[3] Lefebvre, A. H., and Ballal, D. R., 2010, Gas Turbine Combustion: Alternative Fuels and Emissions, 3rd ed., Taylor & Francis, New York, pp. 136–167.

[4] Damkohler, G., 1947, "The Effects of Turbulence on the Flame Velocity in Gas Mixtures, " NACA TM 1112.

[5] Semenov, N. N., 1942, "Thermal Theory of Combustion and Explosion III," NACA TM 1026.

[6] Lefebvre, A. H., 1966, "Theoretical Aspects of Gas Turbine Combustion Performance," CoA Note Aero, No. 163, Cranfield University, UK, pp.1–17.

Acknowledgments

The author would like to extend his deepest gratitude to Professor Toshiyuki Toriyama of Ritsumeikan University for his professional direction, valuable suggestion and in-depth discussion in every aspect of this study.

The author would like to express his gratitude to laboratory members.

Finally, the author would like to extend a special thank you to affectionate and encouragement of his parents.